*J. Fluid Mech.* (2012), *vol.* 710, *pp.* 419–452. © Cambridge University Press 2012 
doi:10.1017/jfm.2012.371

# On the universality of turbulent axisymmetric wakes

**John A. Redford‡, Ian P. Castro and Gary N. Coleman†**

Aerodynamics and Flight Mechanics Research Group, University of Southampton, Highfield, Southampton SO17 1BJ, UK

(Received 22 November 2011; revised 10 May 2012; accepted 18 July 2012; first published online 5 September 2012)

Direct numerical simulations (DNS) of two time-dependent, axially homogeneous, axisymmetric turbulent wakes having very different initial conditions are presented in order to assess whether they reach a universal self-similar state as classically hypothesized by Townsend. It is shown that an extensive early-time period exists during which the two wakes are individually self-similar with wake widths growing like $\delta \propto t^{1/3}$, as predicted by classical dimensional analysis, but have very different growth rates and are thus not universal. Subsequently, however, the turbulence adjusts to yield, eventually, wakes that are structurally identical and have the same growth rate (also with $\delta \propto t^{1/3}$) so provide clear evidence of a universal, self-similar state. The former non-universal but self-similar state extends, in terms of a spatially equivalent flow behind a spherical body of diameter $d$, to a distance of $O(3000d)$ whereas the final universal state does not appear before $O(5000d)$ (and exists despite relatively low values of the Reynolds number and no evidence of a spectral $\kappa^{-5/3}$ inertial subrange). Universal wake evolution is therefore likely to be rare in practice. Despite its low Reynolds number, the flow does not exhibit the sometime-suggested alternative self-similar behaviour with $\delta \propto t^{1/2}$ (as for the genuinely laminar case) at large times (or, equivalently, distances), since the eddy viscosity remains large compared to the molecular viscosity and its temporal variations are not negligible.

**Key words:** shear layer turbulence, turbulence simulation, wakes

## 1. Introduction

The aim of this study is to examine the relationship between the manner in which a turbulent wake is generated and its later development. We are particularly interested in the validity or otherwise of the Townsend (1956) hypothesis that, irrespective of the details of how they are created, all boundary-free turbulent shear flows eventually reach a universal state, determined solely by the integral constraints of mass, momentum and energy conservation (Narasimha 1992) (cf. Narasimha & Prabhu 1972; Sreenivasan 1981; Sreenivasan & Narasimha 1982). This hypothesis is based on the assumption that by the time the turbulence reaches the far field, it will have been subjected to a universal 'eddy scrambling' process that causes it to 'forget' the

† Present address: Computational Aerosciences Branch, NASA Langley Research Center, Hampton, VA 23681, USA. Email address for correspondence: Gary.N.Coleman@nasa.gov

‡ Present address: CMLA, ENS de Cachan, 61 avenue du président Wilson, 94235 Cachan, France.

https://doi.org/10.1017/jfm.2012.371 Published online by Cambridge University Press

near-field characteristics (such as geometry-dependent vortical structures), set by the initial conditions. Townsend's hypothesis thus predicts that all free-shear flows of a given type (e.g. plane jet or axisymmetric wake) will eventually spread at the same rate, and possess turbulence statistics exhibiting the same self-similar profiles (Tennekes & Lumley 1972). Although plausible and conceptually attractive, the idea of universal self-similarity is currently somewhat controversial. Its validity has been called into question, for example, by the measurements of Bevilaqua & Lykoudis (1978), who found that the wakes downstream of two axisymmetric bodies (one a sphere, the other a porous circular disk) were both self-similar but not uniquely so – despite both bodies producing the same drag (see also Zhou & Antonia 1995's plane-wake study). More recently, George and co-authors (George 1989; Johansson, George & Gourlay 2003; George & Davidson 2004; Ewing *et al.* 2007; George 2008) have developed a generalized similarity analysis that accounts for the effect of the details of the initial conditions, in addition to the net momentum, on the asymptotic state of various free-shear flows. They point to the growing body of experimental data and numerical simulation results that show the far-field statistics, such as mean growth rates, remain marked by the manner in which the near-field turbulence was generated. Pope's (2000) summary of far-field axisymmetric wake experiments, each of which used different bodies (porous and solid disks, spheres and ellipsoids), includes self-similar behaviour with streamwise turbulence intensities that on the centreline range from 30 % to over 100 % of the maximum mean velocity deficit $U_d$, and values of the mean spreading parameter $\beta = (U_\infty/U_d)/(\mathrm{d}h/\mathrm{d}x)$ (where $U_\infty$ is the free-stream velocity and $h$ the wake half-width) from less than 0.1 to 0.8, for the various cases. It thus appears that the shape of a body does have a lasting effect on the wake turbulence far downstream, in regions where self-similarity is present.

However, the possibility that the initial-condition dependence eventually fades cannot be ruled out. In fact, Bevilaqua & Lykoudis stress the difference between universality (their 'equilibrium') and self-similarity (their 'self-preservation'), suggesting non-universal forms of the latter may in time tend asymptotically towards the former. Moreover, Narasimha (1992) notes 'conflicting evidence from different experiments suggests that there may be multiple metastable equilibrium states' present in turbulent shear flows.

The question of universality is examined here by comparing 'far field' (i.e. late) results from direct numerical simulation (DNS) of two time-developing axisymmetric wake flows, initialized such that they contain distinctly different turbulence structures but the same net momentum defect. In this sense, this study can be viewed as a computational counterpart of the Bevilaqua & Lykoudis experiments. It is also a higher-Reynolds-number, larger-domain, version of the DNS of Basu, Narasimha & Sinha (1992). (Because the present flow spreads laterally with time, not downstream distance, it is parallel in the mean, and thus, due to Galilean invariance, is equivalent to a time-developing axisymmetric co-flowing jet. The term 'wake' will be used henceforth in a generalized sense, to include flows with 'deficits' of either sign.) In what follows, evidence is presented for the existence of Narasimha's metastable states, characterized by non-universal (initial-condition-dependent) self-similarity, that eventually give way to the universal self-similarity anticipated by Townsend.

In § 2, the major features of self-similarity and universality for the present flow are addressed. Section 3 describes the numerical approach and the two initialization strategies. Section 4 contains the results, where wake features are examined for the periods over which the flows are self-similar but not universal (early times, § 4.1) and universal (late times, § 4.2). Conclusions are summarized in § 5.

https://doi.org/10.1017/jfm.2012.371 Published online by Cambridge University Press

## 2. Self-similarity and universality

Since the time-dependent axisymmetric wake is homogeneous in both the azimuthal and axial directions, the continuity equation leads directly to a zero mean radial velocity, $\overline{v}_r = 0$. (An overbar is used throughout to indicate a streamwise and azimuthal average, such that all mean quantities depend on both radial distance $r$ from the symmetry axis and time $t$.) Volume integration of the streamwise momentum equation shows that the volume-flux deficit $I_d = 2\pi \int_0^\infty Ur\,\mathrm{d}r$ is constant with time, where the mean streamwise velocity $\overline{v}_x(r,t) = -U(r,t)$, with $U = U_d$ at $r = 0$ and $U \to 0$ as $r \to \infty$. In a spatially developing wake, $U$ would be the difference between the free-stream velocity $V_\infty$ and $\overline{v}_x(r)$. Self-similarity is possible in such wakes only if this deficit velocity is very much smaller than $V_\infty$, so it is in that sense (in contrast to some other classical shear flows) only an asymptotically correct solution. (Recall that another consequence of the $U_d \ll V_\infty$ condition for the spatial case is that the constant-momentum constraint is equivalent to conservation of $I_d$.) The spatial wake is thus the exact converse of the asymptotic jet in a co-flowing stream, which has a negative $U_d$. The common case of an axisymmetric jet issuing into still air does not have a homogeneous time-dependent equivalent; it is only the jet in a co-flow that does (for small jet velocity excess), and all time-dependent parallel-flow idealizations of it are, just like their spatial equivalents, wake-like. Because the mean velocity of the time-developing wake is parallel, the magnitude of the free-stream velocity is irrelevant; we choose $V_\infty = 0$. The present case can thus be viewed as a time-developing analogue to the far wake generated by an axisymmetric body moving into quiescent fluid. Whether or not this flow can be self-similar depends only on whether the scaled equations of motion allow it and whether there is enough time for any crucial 'non-wake-like' features of the initial conditions to be forgotten. We return to this latter point in due course.

For the present idealization, the mean axial momentum equation is given by

$$\frac{\partial \overline{v}_x}{\partial t} = \frac{1}{r}\frac{\partial}{\partial r}\left[r\left(-\overline{v_x' v_r'} + \nu\frac{\partial \overline{v}_x}{\partial r}\right)\right], \tag{2.1}$$

where $\nu$ is the kinematic molecular viscosity and primed quantities denote, as usual, deviations from the mean. Assuming self-similarity and thus writing, in the usual way,

$$U = U_d(t) f(\eta), \tag{2.2}$$

$$-\overline{v_x' v_r'} = R_s(t) g(\eta), \tag{2.3}$$

where $\eta = r/\delta(t)$ is the radial similarity coordinate and $\delta$ a measure of the wake width, (2.1) becomes

$$\left[\frac{\delta}{U_d^2}\frac{\mathrm{d}U_d}{\mathrm{d}t}\right] f - \left[\frac{1}{U_d}\frac{\mathrm{d}\delta}{\mathrm{d}t}\right]\eta f_\eta = -\left[\frac{R_s}{U_d^2}\right]\left(g_\eta + \frac{g}{\eta}\right) + \left[\frac{\nu}{U_d\,\delta}\right]\left(f_{\eta\eta} + \frac{f_\eta}{\eta}\right), \tag{2.4}$$

where $f_\eta = \mathrm{d}f/\mathrm{d}\eta$, $f_{\eta\eta} = \mathrm{d}^2 f/\mathrm{d}\eta^2$ and $g_\eta = \mathrm{d}g/\mathrm{d}\eta$. Similarly, $I_d$ can be expressed by

$$\frac{I_d}{2\pi} = \left[U_d\,\delta^2\right]\int_0^\infty f\eta\,\mathrm{d}\eta, \tag{2.5}$$

showing that (since $I_d$ is constant) $U_d \propto \delta^{-2}$.

In (2.4) the square-bracketed terms contain all the explicit time-dependence. Following Johansson *et al.* (2003) (hereinafter referred to as JGG), and Moser, Rogers & Ewing (1998), the shear-stress scaling parameter $R_s$ is not assumed to be $U_d^2$, as was usual in some of the early classical analyses (Tennekes & Lumley 1972, for example),

https://doi.org/10.1017/jfm.2012.371 Published online by Cambridge University Press

although Townsend (1976) did not make this assumption. If it is assumed that the Reynolds number $Re$ is sufficiently large that the viscous terms can safely be ignored, then (2.4) requires that

$$\left[\frac{\delta}{U_d^2}\frac{\mathrm{d}U_d}{\mathrm{d}t}\right] \propto \left[\frac{1}{U_d}\frac{\mathrm{d}\delta}{\mathrm{d}t}\right] \propto \left[\frac{R_s}{U_d^2}\right]. \tag{2.6}$$

The constant-$I_d$ condition ensures that the first two terms are automatically proportional to each other. JGG point out that the third term is proportional to the first two provided $R_s \propto \beta U_d^2$, where $\beta = (1/U_d)\,\mathrm{d}\delta/\mathrm{d}t$ is (the time-developing version of) the mean growth/spreading rate of the wake. Consequently, the axial Reynolds-averaged Navier–Stokes (RANS) equation will exhibit universal form only if the Reynolds shear stress $-\overline{v_x' v_r'}$ scales in a universal manner with $\beta U_d^2$ (see also Moser *et al.* 1998). This reveals how mean-flow profiles from wakes with different growth rates can (and suggests why they often do) show the same, universal variation when plotted in traditional similarity coordinates (i.e. scaled by $U_d$ and $\delta$), while the Reynolds-stress profiles, scaled by $U_d^2$ alone, do not (cf. George 1989; Moser *et al.* 1998).

Writing $\delta \propto t^n$ and $R_s \propto t^m$ (so that $U_d \propto t^{-2n}$ and $R_s \propto t^{-(n+1)}$), then assuming $\beta$ is constant, leads (since $\beta \propto t^{3n-1}$) to the classical solution in which $n = 1/3$ and $m = -4/3$. If constant $\beta$ is not assumed *a priori,* the $n = 1/3$ solution can also be obtained by neglecting the viscous terms and considering the Reynolds-stress equations (JGG); these imply that the normal Reynolds stresses (e.g. $\overline{v_x' v_x'}$) are all proportional to $U_d^2 \propto t^{-4/3}$.

The $n = 1/3$ solution also follows directly from the Townsend hypothesis, which amounts to assuming that the $U_d(t)$ evolution solely depends on $I_d$ and $t$, leading via dimensional analysis to the condition $U_d \propto I^{1/3} t^{-2/3}$, or

$$U_d = C_T I_d^{1/3}\,(t - t_{vo})^{-2/3}, \tag{2.7}$$

where $C_T$ is (within this assumption) a universal constant and $t_{vo}$ a (non-universal) virtual offset time. Determining the validity of (2.7) – and in particular whether, and if so under what conditions, $C_T$ is universal – is a central objective of this study.

The mean local Reynolds number $U_d\,\delta/\nu$ is proportional to $t^{-n}$, while the ratio of the time-dependent coefficients of the Reynolds- and viscous-stress terms in (2.4), $[R_s/U_d^2]/[\nu/U_d\,\delta]$, scales as $t^{2n-1}$. With $n = 1/3$, both quantities decrease with time. (Note that if $n = 1/2$, the latter ratio would be constant in time; this possibility is considered below.) Eventually therefore viscous effects must become significant.

It could be argued that the nature of the turbulence within the wake is controlled by a Reynolds number based on the turbulence quantities. Defining a turbulence velocity scale by $k^{1/2}$ and an appropriate large-eddy scale by $\ell = k^{3/2}/\epsilon$, where $k$ is the turbulence kinetic energy and $\epsilon$ is its dissipation rate, a common turbulence Reynolds number is $Re_\ell = k^2/\epsilon\nu$. For high Reynolds number, this quantity varies like $t^{-1/3}$, so, again, one would expect the finite/low-Reynolds-number solution ($n = 1/2, m = -3/2$) to appear eventually. (The Reynolds number based on the Taylor microscale, $Re_\lambda$, varies like $(Re_\ell)^{1/2}$, and therefore also falls, but more slowly, as $t^{-1/6}$.)

If the analysis is repeated for finite $Re$, the momentum equation on its own is sufficient to give $n = 1/2$ (by adding the fourth of the square-bracketed terms in (2.4) to the similarity conditions (2.6)). There are two possibilities: (*a*) the turbulence and viscous terms are of the same order (as assumed in JGG) and (*b*) the flow is purely laminar (such that $R_s \equiv 0$). The former will presumably first be encountered as the

https://doi.org/10.1017/jfm.2012.371 Published online by Cambridge University Press

flow leaves the high-*Re* $n = 1/3$ regime. (An $n = 1/2$ solution characterized by large turbulence-to-viscous stress ratio, such that $\nu_t/\nu > O(1)$, is also possible, but only if the eddy viscosity $\nu_t \equiv -\overline{v_x' v_r'}/(\partial \overline{v}_x/\partial r)$ is constant with respect to time; see below. The DNS results presented here do not support this possibility, except as an anomalous and early temporary state for one of the cases.)

There is a qualitative difference between the large-Reynolds-number and the first $n = 1/2$ solutions, associated with the $t^{2n-1}$ scaling found above for the ratio of the time-dependent coefficients of the turbulent and viscous terms in (2.4). This shows that $\nu_t$ is also proportional to $t^{2n-1}$, such that $\nu_t/U_d\,\delta \propto t^{3n-1}$. For high *Re* ($n = 1/3$), $\nu_t/\nu$ will thus decrease as $t^{-1/3}$, while for $n = 1/2$ it will be constant. Therefore, if the shear-stress similarity function $g(\eta)$ (and thus (2.4)) were to maintain its form for all time after the flow entered the first $n = 1/2$ similarity regime, an initially fully turbulent axisymmetric wake would, as $U_d \to 0$, always possess turbulent stresses that are never identically zero, and therefore would never become purely laminar. JGG argue that this will happen. We will not be able to settle the question here. (When run long enough, the present simulations eventually become fully laminar at very late times – corresponding to millions of diameters downstream of a virtual wake-generating body – but this is solely a consequence of the very late wake's size becoming too large for the streamwise domain. We cannot at present say whether the turbulence would completely die if it were in a domain that was much larger than the ones used here.) Our primary focus will instead be upon the $n = 1/3$ regime, which turns out to be unexpectedly robust and long lived.

## 3. Numerical approach and parameters

In order to distinguish between the detailed and bulk/integral characteristics of the initial conditions, and thereby allow a straightforward test of Townsend's hypothesis, we compare two incompressible axisymmetric wake flows with distinctly different initial turbulence structure but identical initial mean-velocity deficit profiles (corresponding to wakes downstream of two distinctly shaped axisymmetric bodies with identical drag). The objective is not, per se, to mimic specific wake flows (by for example using particular laboratory measurements to define the initial conditions), but rather to perform a numerical experiment involving two flows whose initial states contain significant well-defined structural differences. The streamwise homogeneity associated with the use of the parallel-flow idealization to create wakes that develop in time, rather than space, allows efficient DNS with a standard triply periodic FFT-based pseudo-spectral method (Gottlieb & Orszag 1977).

The pressure variable in the Navier–Stokes equations is eliminated using a velocity–vorticity formulation (Kim, Moin & Moser 1987). A low-storage third-order temporal discretization (Spalart, Moser & Rogers 1991) is applied to the nonlinear terms, while the viscous terms are treated analytically (Rogallo 1981). In what follows, $x = x_1$ corresponds to the streamwise direction, along the wake axis, while $y = x_2$ and $z = x_3$ are the two lateral coordinates (for illustration purposes, $z$ will be aligned in the vertical direction, while $x$–$y$ planes are horizontal).

The first initialization strategy (denoted VR) induces a nonlinear/bypass transition, by specifying a series of vortex rings and perturbing them slightly, via radial/geometric displacement of the core location. The initial Case VR field is illustrated by the vorticity contours in figure 1(*a*) and the streamwise velocity spectrum in figure 2(*a*) (dotted line). This initial field corresponds to the time just after a virtual body has 'passed' through the domain, with the ensuing flow (conceptually) 'straightened' to

https://doi.org/10.1017/jfm.2012.371 Published online by Cambridge University Press

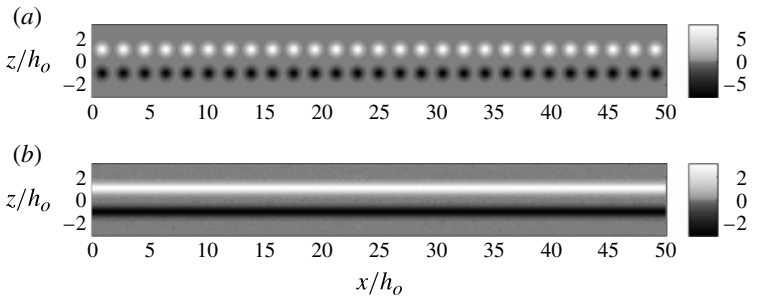


FIGURE 1. Initial vorticity contours for (*a*) Case VR, and (*b*) Case SD. Vorticity component into the page in the vertical plane containing the wake centreline, non-dimensionalized by the maximum mean velocity in the plane and the vortex-ring diameter. Plots show the full initial lateral domain for both cases, but only one quarter of the streamwise domain for Case VR, and one eighth for Case SD.

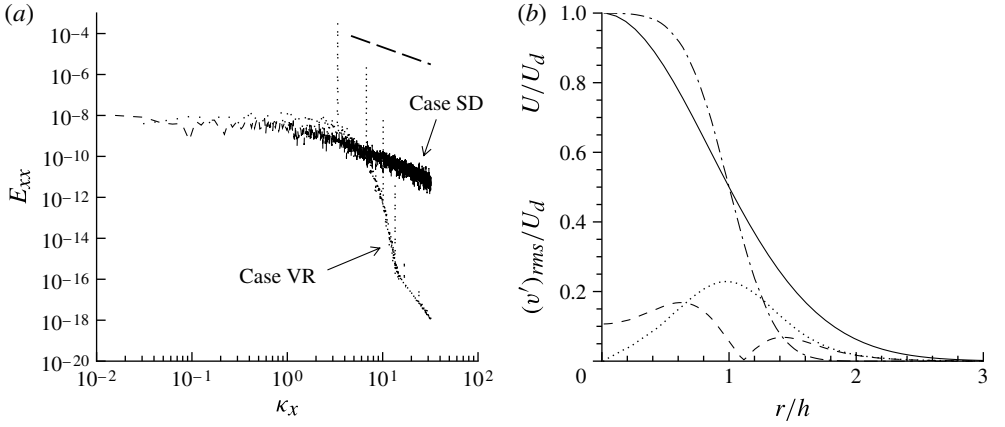


FIGURE 2. Initial conditions. (*a*) One-dimensional streamwise energy spectra $E_{xx}$ at $r = h$: ·····, Case VR; - - - -, Case SD; – – – –, $\kappa_x^{-5/3}$ behaviour. Results non-dimensionalized by $h_o$ and $U_r = 1.86U_{do}$. (*b*) Velocity profiles: – · –, $U/U_d$ for Cases VR and SD; —, $U/U_d = \exp(-\ln(2)\,(r/h)^2)$; - - - -, $(\overline{v_x' v_x'})^{1/2}$ for Case VR; ·····, $(\overline{v_r' v_r'})^{1/2}$ for Case VR. Velocity fluctuations for Case SD are too small to be visible in this plot.

produce streamwise homogeneity, thus allowing convective changes to be replaced by temporal ones.

Following Shariff, Verzicco & Orlandi (1994), each ring in the sequence is represented as a Gaussian distribution of azimuthal core vorticity $\omega_\theta$, such that $\omega_\theta = (\Gamma/\pi\delta_\omega^2)\exp[-(s/\delta_\omega)^2]$, where $s^2 = (x - x_c)^2 + (r - R)^2$, with $r^2 = (y - y_c)^2 + (z - z_c)^2$ and $R$ the radius of the ring measured from $(x_c, y_c, z_c)$ (the location of the centre of the ring in question, on the wake axis), and $\delta_\omega$ is a length scale defining the thickness of the vortex core (chosen as $\delta_\omega = 0.4R$). The circulation $\Gamma = \int \omega_\theta \mathrm{d}S$, where $S$ is in an $x$–$r$ plane that bisects the ring. The rings are spaced uniformly every $16\pi R/27$ along the wake axis (figure 1*a*). They induce the mean streamwise profile $U(r)$ shown by the chained-dotted curve in figure 2(*b*), such that the net defect $I_d = 3.395U_{do}h_o^2$, where $U_{do}$ and $h_o$ are, respectively, the initial centreline velocity and the initial mean-velocity

https://doi.org/10.1017/jfm.2012.371 Published online by Cambridge University Press

half-width (more accurately 'half-radius') $h_o$, which is the radial distance from the wake axis to the point at which $U(r) = 0.5U_d$. Note that $h_o$ is equivalent to the radius of the individual rings. (Consider the net streamwise velocity induced by the vorticity within a rectangular $r$–$x$ contour extending from $r = 0$ to $r = R$.) The $U(r)$ variation differs somewhat from the Gaussian idealization (shown as the solid curve in figure 2*b*). The corresponding velocity-fluctuation profiles given by the chain of rings are shown in figure 2(*b*) (dashed and dotted curves). The initial mean wake Reynolds number $U_d h/\nu$ is 2950.

This initialization leads to turbulence by way of the azimuthal instability of each ring, which is triggered by a $0.004R$ maximum displacement of the ring radius for each of the azimuthal modes 5–32, with random azimuthal phases (with different random-number seeds for each ring). (Including modes 1–4 causes the rings to diverge away from the wake centreline, preventing the formation of a coherent wake flow; neglecting these lower modes allows each ring to interact with its neighbour such that when they break down, the turbulent structures shed into the individual vortex-ring wakes pass into the centre of the following ring.) For the present slenderness ratio, $\delta_\omega/R = 0.4$, modes 5–7 are most amplified (Shariff *et al.* 1994). The ensuing ring breakdown is reminiscent of results in Archer, Thomas & Coleman (2008), although the breakdown process is modified, compared to the isolated ring case, because of the influence of the neighbouring rings (both because of the ejection of vortical structures by each ring and the alterations to the total strain field (Archer *et al.* 2008)). Here the breakdown of the vortex rings is quicker than the isolated ring case. Nevertheless, as for the isolated ring, mode 6 is most amplified. (See figure 5*a*, below.)

The other initialization strategy (Case SD, for 'small disturbances') adds very low-level random-phase velocity fluctuations to the axisymmetric mean-velocity profile taken from Case VR, so that the ensuing wake turbulence is the result of growth and interaction of the linearly unstable modes of the parallel-flow axisymmetric shear layer. Each non-zero Fourier mode for each velocity component was assigned the value $10^{-3}\, U_r/(\kappa_x^2 + \kappa_y^2 + \kappa_z^2)h_o^2$, where the reference velocity $U_r = 1.86U_{do}$ and $\kappa_x$, $\kappa_y$ and $\kappa_z$ are the components of the cartesian wavevector. This is not consistent with a divergence-free field but, although producing such a field would be possible, there is nothing to be gained since continuity is immediately enforced by the code. This approach is similar to that employed by Gourlay *et al.* (2001) and Dommermuth *et al.* (2002), apart from the fact that they used large-amplitude disturbances, which triggered a (synthetic) nonlinear bypass transition. (The large-eddy simulations (LES) of Dommermuth *et al.* (2002) utilized initial disturbances with maximum root-mean-squared velocity fluctuations of $0.055U_d$. The initial energy levels for the Gourlay *et al.* (2001) DNS can be inferred from the cross symbols shown in figure 11*a*, below.) Here the maximum turbulence kinetic energy of the radial initial-disturbance profile is $3 \times 10^{-6}\, U_{do}^2$. The differences and similarities of the Case VR and SD initializations are summarized in figures 1 and 2. Note that while the mean profiles $U(r)$ are identical for the two cases, the initial velocity fluctuations for Case SD are negligible compared to those for Case VR, shown in figure 2(*b*).

One of the computational challenges associated with this flow is defining an appropriate domain. The domain size directly affects the quality of the mean statistics, which for this time-developing parallel flow are obtained by sampling over the streamwise direction $0 \leqslant x \leqslant \Lambda_x$, and azimuthally over $0 \leqslant \theta \leqslant 2\pi$ at fixed radius $r$. (Ensemble averages of multiple realizations are also possible, although not employed in the present study.) As the wake ages and spreads, the size of the 'large-eddy sample' will decrease, causing greater uncertainty in statistics. Consequently, we use

https://doi.org/10.1017/jfm.2012.371 Published online by Cambridge University Press

a relatively large (fixed) streamwise domain, with $\Lambda_x/h_o = 64\pi \approx 201$ for Case VR (comparable to Gourlay *et al.*'s 245) and $\Lambda_x/h_o = 128\pi \approx 402$ for Case SD. Choosing a larger $\Lambda_x$ for Case SD (which, as we shall see, contains larger eddy structures during its early development relative to those found in Case VR) produces statistics whose uncertainty for both cases is comparable (see figure 15*b*). It also allows a straightforward demonstration that the results are not affected by $\Lambda_x$. These streamwise domains are large enough to accommodate the full range of times given in tables 1 and 2 without artificially altering the wake evolution. Even at the latest times considered ($t/t_* \approx 31\,000$, where $t_* = \rho_{*o}/U_{do}$ and $\rho_{*o}$ is the initial value of the integral width scale defined in (4.1)), $\Lambda_x$ contains 8.5 and 17 streamwise integral length scales for Cases VR and Case SD, respectively; see § 4.2 for details. (Case VR and SD results at $t/t_* \approx 31\,000$ were the latest that are deemed to be physically meaningful. Case VR was continued until $t/t_* = 5.5 \times 10^6$, but only to illustrate the constraining influence of the streamwise domain, which eventually leads to a numerically induced fully laminar state (cf. figure 16*a*).)

Of even greater concern is the possibility that the wake will outgrow the periodic lateral domain. To avoid this problem without unduly wasting computational resources, the lateral domain size $\Lambda_z = \Lambda_y$ is dynamically increased by projecting the periodic solutions onto a domain of greater extent with the same grid spacing (i.e. maximum wavenumber). Following T. S. Lund (personal communication), we place the dependent variables from the smaller domain at the centre of the new one, surrounded by reference values from the original boundaries. This involves defining the variables $\boldsymbol{u}$ in physical space using a windowing function $f_l$ such that their new values $q_i(j,l,m) = u_i(x_j, y_l, z_m)$ (with $x_j = j\Lambda_x/N_x$, $y_l = l\Lambda_y/N_y$ and $z_m = m\Lambda_z/N_z$, for $j = (1, 2, \ldots, N_x)$, $l = (1, 2, \ldots, N_y)$ and $m = (1, 2, \ldots, N_z)$) are given by $q_i(j,l,m) = (q_i^\star - \widehat{q}_i) f_l f_m + \widehat{q}_i$, where $f_l = (1/2)[\tanh((a_l + N_y^\star/2)/5) - \tanh((a_l - N_y^\star/2)/5)]$, with $a_l = l - (N_y + 1)/2$, and where $N_y = N_z = 3M_y/2 = 3M_z/2$ is the number of lateral collocation/grid points, $l = (1, 2, \ldots, N_y)$ is the lateral grid-point index, and $^\star$ denotes the old variable or grid size; the edge values $\widehat{q}_i$ are defined as the average of $u_i^\star$ over the streamwise-lateral ($x, y$ and $x, z$) faces of the old domain. This procedure sets the dependent variables at the edges of the new domain to constant reference values, thereby maintaining their lateral periodicity.

The changes made to $\Lambda_z = \Lambda_y$ for Cases VR and SD are shown in tables 1 and 2. The value of $\Lambda_z$ below which the wake evolution would be compromised is a surprisingly small multiple of the wake width. This can be deduced from figure 3(*a*), where Case VR results beginning from a fresh domain expansion (at $t/t_* = 183$) are compared to those from an otherwise identical simulation for which $\Lambda_z = \Lambda_y$ remained fixed at its earlier, smaller value, imposed at $t/t_* = 136$. The time at which the results diverge (contrast the lines and symbols) indicates that the critical value is $\Lambda_z \approx h/0.17 \approx 5.9h$ (based on the time at which the streamwise velocity fluctuations at the edge of the wake, $r = 2h$, from the fixed domain (open square symbols) first deviate from the larger-domain benchmark). As shown in tables 1 and 2, apart from two brief exceptions during the beginning of Case SD ($t/t_* < 60$), the lateral domain size is above (usually well above) this value for the entire history of both cases.

Throughout this paper overbars (as in $\overline{v_x' v_x'}$) denote quantities that have been averaged both axially and azimuthally, angle brackets (as in $\langle v_i \rangle$) denote quantities averaged only axially (such that $\langle v_i \rangle = \int_0^{\Lambda_x} v_i \, \mathrm{d}x/\Lambda_x$) and braces (as in $\{\widetilde{P}_k\}$) denote (axially averaged) quantities integrated over the entire lateral $(y, z)$ domain. So, for example, the usual turbulence kinetic energy $k$ is $(1/2)\overline{v_i' v_i'}$, while its area-integrated

https://doi.org/10.1017/jfm.2012.371 Published online by Cambridge University Press

| $t/t_*$ | $M_x$ | $\Delta x/\eta_{min}$ | $M_z$ | $\Delta z/\eta_{min}$ | $\Lambda_z/h_o$ | $h/\Lambda_z$ | $I_d/I_{do}$ |
|---|---|---|---|---|---|---|---|
| 0 | 2048 | 0.5 | 128 | 0.3 | $2.0\pi$ | 0.159 | 1 |
| 21 | | 4.8 | | 2.4 | | 0.161 | 1.0000 |
| 32 | | 7.2 | 192 | 2.4 | | 0.146 | 1.0000 |
| 32 | | | 256 | | $2.67\pi$ | 0.110 | |
| 35 | 2560 | 5.3 | | 2.2 | | 0.119 | 1.0000 |
| 37 | 3072 | 4.2 | 192 | 2.8 | | 0.124 | 1.0000 |
| 39 | | 3.9 | | 2.6 | | 0.129 | 1.0000 |
| 39 | | | 256 | | $3.56\pi$ | 0.097 | |
| 45 | | 3.5 | 192 | 3.1 | | 0.105 | 1.0000 |
| 51 | | 3.2 | | 2.9 | | 0.112 | 1.0000 |
| 51 | | | 256 | | $4.74\pi$ | 0.084 | |
| 89 | | 2.1 | 192 | 2.5 | | 0.120 | 1.0001 |
| 89 | | | 256 | | $6.32\pi$ | 0.090 | |
| 102 | 2560 | 2.3 | | 2.3 | | 0.096 | 1.0001 |
| 136 | 2048 | 2.3 | 192 | 2.4 | | 0.113 | 1.0001 |
| 136 | | | 256 | | $8.43\pi$ | 0.085 | |
| 183 | | 1.9 | 192 | 2.7 | | 0.098 | 1.0001 |
| 183 | | | 256 | | $11.24\pi$ | 0.073 | |
| 837 | 1536 | 0.9 | 192 | 1.3 | | 0.139 | 1.0002 |
| 837 | | | 256 | | $14.98\pi$ | 0.104 | |
| 1507 | 1024 | 0.9 | 192 | 1.2 | | 0.129 | 1.0005 |
| 1507 | | | 256 | | $19.88\pi$ | 0.097 | |
| 2242 | 768 | 0.9 | 192 | 1.2 | | 0.113 | 1.0005 |
| 2242 | | | 256 | | $26.64\pi$ | 0.085 | |
| 4545 | 512 | 0.9 | 192 | 1.0 | | 0.119 | 1.0006 |
| 4545 | | | 256 | | $35.52\pi$ | 0.089 | |
| 6961 | 384 | 0.9 | 192 | 1.0 | | 0.103 | 1.0006 |
| 6961 | | | 256 | | $47.35\pi$ | 0.077 | |
| 15542 | 256 | 0.8 | 192 | 0.8 | | 0.097 | 1.0007 |
| 15542 | | | 256 | | $63.14\pi$ | 0.073 | |
| 20272 | 192 | 1.0 | 192 | 1.0 | | 0.076 | 1.0007 |
| 30964 | | 0.7 | | 0.7 | | 0.093 | 1.0007 |

TABLE 1. Case VR numerical parameters. The numbers of streamwise $M_x$ and lateral $M_z = M_y$ Fourier-expansion coefficients are two-thirds of the corresponding collocation/quadrature grid points: $N_x = 3M_x/2$ and $N_z = N_y = 3M_z/2 = 3M_y/2$. Streamwise $\Delta x$ and lateral $\Delta z = \Delta y$ grid spacings given by $\Lambda_x/N_x$ and $\Lambda_z/N_z$, respectively. Minimum Kolmogorov length scale $\eta_{min} = (\nu^3/\epsilon_{max})^{1/4}$, where $\epsilon_{max}$ is the maximum of the streamwise/azimuthal-mean rate of dissipation of turbulence kinetic energy at each time. The length $\Lambda_x$ of the streamwise domain is fixed at $64\pi h_o$, while the size $\Lambda_z = \Lambda_y$ of the square lateral domain increases at times shown (indicated by vertical gaps between rows). Values remain unchanged until a new entry is given. Times non-dimensionalized by $t_* = \rho_{*o}/U_{do}$. Initial volume-flux defect $I_{do} = 3.395 U_{do} h_o^2$.

https://doi.org/10.1017/jfm.2012.371 Published online by Cambridge University Press

| $t/t_*$ | $M_x$ | $\Delta x/\eta_{min}$ | $M_z$ | $\Delta z/\eta_{min}$ | $\Lambda_z/h_o$ | $h/\Lambda_z$ | $I_d/I_{do}$ |
|---|---|---|---|---|---|---|---|
| 0 | 4096 | 0.7 | 128 | 0.4 | 2.0π | 0.159 | 1 |
| 25 | 5120 | 1.6 | 192 | 0.7 | | 0.158 | 1.0000 |
| 40 | 6144 | 2.6 | | 1.3 | | 0.167 | 0.9999 |
| 43 | | 2.8 | | 1.4 | | 0.178 | 0.9999 |
| 43 | | | 256 | | 2.67π | 0.133 | |
| 49 | | 3.1 | 192 | 2.1 | | 0.160 | 1.0019 |
| 49 | | | 256 | | 3.56π | 0.120 | |
| 58 | | 3.5 | 192 | 3.1 | | 0.195 | 1.0027 |
| 58 | | | 256 | | 4.74π | 0.146 | |
| 63 | | 3.3 | 192 | 3.9 | | 0.170 | 1.0028 |
| 63 | | | 256 | | 6.32π | 0.127 | |
| 90 | 5120 | 2.4 | 192 | 3.1 | | 0.160 | 1.0029 |
| 90 | | | 256 | | 8.43π | 0.120 | |
| 154 | 4096 | 1.8 | 192 | 2.5 | | 0.150 | 1.0030 |
| 154 | | | 256 | | 11.24π | 0.113 | |
| 242 | | 1.3 | 192 | 2.4 | | 0.131 | 1.0030 |
| 242 | | | 256 | | 14.98π | 0.099 | |
| 366 | 3072 | 1.3 | | 1.8 | | 0.107 | 1.0031 |
| 453 | 2560 | 1.3 | | 1.5 | | 0.110 | 1.0031 |
| 552 | 2048 | 1.4 | 192 | 1.8 | | 0.113 | 1.0031 |
| 552 | | | 256 | | 19.98π | 0.085 | |
| 1025 | 1536 | 1.3 | 192 | 1.6 | | 0.104 | 1.0031 |
| 1025 | | | 256 | | 26.64π | 0.078 | |
| 2105 | 1024 | 1.3 | 192 | 1.4 | | 0.099 | 1.0031 |
| 2105 | | | 256 | | 35.52π | 0.074 | |
| 4417 | 768 | 1.1 | 192 | 1.2 | | 0.089 | 1.0031 |
| 4417 | | | 256 | | 47.35π | 0.067 | |
| 8413 | 512 | 1.2 | 192 | 1.2 | | 0.084 | 1.0030 |
| 8413 | | | 256 | | 63.14π | 0.063 | |
| 15671 | 384 | 1.1 | 192 | 1.1 | | 0.081 | 1.0031 |
| 15671 | | | 256 | | 84.18π | 0.061 | |
| 27146 | 256 | 1.2 | 192 | 1.0 | | 0.071 | 1.0031 |
| 27146 | | | 256 | | 112.25π | 0.053 | |
| 30920 | | 1.1 | | 0.9 | | 0.055 | 1.0031 |

TABLE 2. Case SD numerical parameters. The length $\Lambda_x$ of the streamwise domain is fixed at $128\pi h_o$. See table 1 for variable definitions.

value $K$ is $(1/2)\{\langle v_i' v_i' \rangle\} = (1/2)\int_0^{\Lambda_z}\int_0^{\Lambda_y}\langle v_i' v_i' \rangle \mathrm{d}y\,\mathrm{d}z)$. (For convenience, a prime is used to indicate deviations from both (full) axial–azimuthal and (partial) axial averages, which in the $\Lambda_x \to \infty$ limit are identical.)

Because the Reynolds number falls continuously, the resolution requirements for this flow become less stringent with time, as the highest-wavenumber modes contain less

https://doi.org/10.1017/jfm.2012.371 Published online by Cambridge University Press

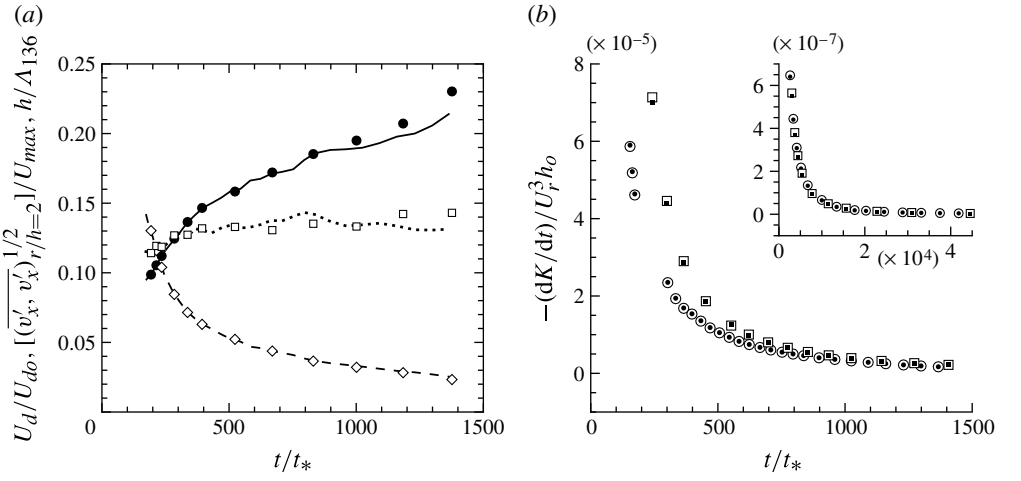


FIGURE 3. (*a*) Comparison of results from Cases VR and VRfd (fixed-lateral-domain run beginning from Case VR field at $t/t_* = 183$, with $\Lambda_z = \Lambda_y$ maintained at $\Lambda_{136} = 8.43\pi h_o$; see table 1): lines, Case VR; symbols, Case VRfd (----/◇, $U_d$; —/●, $h$; ·····/□, $[\overline{(v'_x v'_x)}^{1/2}_{r/h=2}]/U_{max}$ (i.e. root-mean-square streamwise velocity fluctuations near the edge of the wake, at $r = 2h$), where $U_{max}$ is the maximum over the lateral ($y$–$z$) plane) of the axially averaged velocity $\langle u \rangle$. (*b*) Histories of rate of change of area-integrated turbulence kinetic energy $K = (1/2)\{\langle v'_i v'_i \rangle\}$ and net production minus dissipation $\{\widetilde{P}_k\} - \{\widetilde{\epsilon}_k\}$, where $\widetilde{P}_k = -\langle v'_i v'_j \rangle \partial \langle v_i \rangle / \partial x_j$, $\widetilde{\epsilon}_k = \nu \langle s'_{ij} s'_{ij} \rangle$ with $s'_{ij} = (1/2)(\partial v'_i/\partial x_j + \partial v'_j/\partial x_i)$. Case VR: ○, $-\mathrm{d}K/\mathrm{d}t$; ●, $-(\{\widetilde{P}_k\} - \{\widetilde{\epsilon}_k\})$. Case SD: □, $-\mathrm{d}K/\mathrm{d}t$; ■, $-(\{\widetilde{P}_k\} - \{\widetilde{\epsilon}_k\})$. Reference velocity $U_r$ used in (*b*) given by $U_r = 1.86 U_{do}$.

and less energy. Therefore, as the wake develops, some of the highest Fourier modes are removed (see tables 1 and 2). The number of modes that can be removed is greater than the amount added as a result of the domain expansion, so the simulation becomes less costly as time passes. A summary of the number of streamwise $M_x$ and lateral $M_z = M_y$ expansion coefficients used at each time is included in tables 1 and 2. To avoid aliasing errors, the number of physical-space grid (i.e. collocation or quadrature) points in each direction, $N_x$ and $N_z = N_y$, is one-and-a-half times the corresponding number of expansion coefficients.

The validity of the numerical parameters used here is supported by the premultiplied one-dimensional streamwise energy spectra in figure 4, for the streamwise velocity fluctuations $\overline{v'_x v'_x}$ at $r = h$, at times ranging from the beginning to the end of both Cases VR and SD. The low-wavenumber behaviour reflects the initially very small ratio of the size of largest turbulent scales to that of the streamwise domain. The tendency for this ratio to increase in time (corresponding to the increased statistical uncertainty mentioned earlier), and for the turbulence Reynolds number to decrease, can be seen in the relatively more rapid erosion of the energy at higher wavenumbers.

The fall-off of the high-wavenumber end of the figure 4 spectra (spanning as many as ten orders of magnitude) underlines the suitability of the streamwise spatial resolution. This is borne out by the fact that the streamwise $\Delta x$ and lateral $\Delta z = \Delta y$ grid spacings are of the order of the minimum Kolmogrov length scale (defined by the maximum rate of (streamwise–azimuthal) mean turbulence kinetic energy

https://doi.org/10.1017/jfm.2012.371 Published online by Cambridge University Press

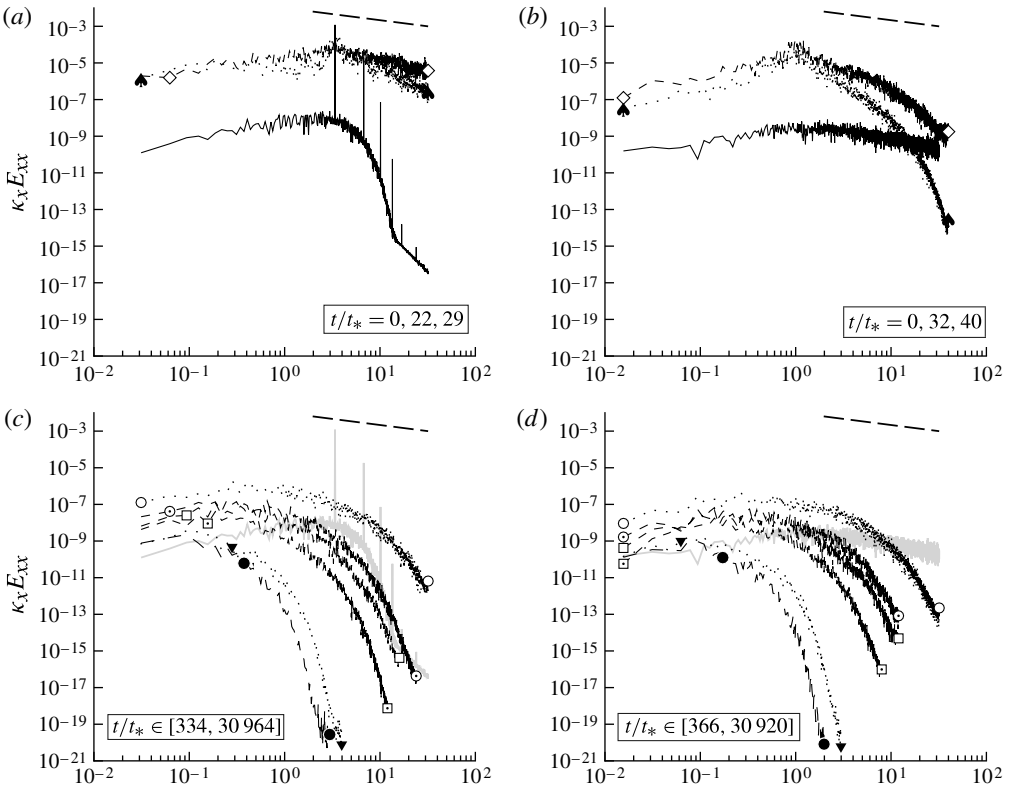


FIGURE 4. Pre-multiplied one-dimensional streamwise energy spectra $E_{xx}$ at $r = h$: —, initial condition, $t = 0$ (shaded in $c$ and $d$); – – – –, $\kappa_x^{-2/3}$ behaviour. Results non-dimensionalized by $h_o$ and $U_r = 1.86U_{do}$. Symbols denote $t/t_*$ values. ($a$) Case VR: ♠, 22; ◇, 29. ($b$) Case SD: ♠, 32; ◇, 40. ($c$) Case VR: ○, 334; ⊙, 1299; □, 2135; ⊡, 4386; ▼, 20 272; ●, 30 964. ($d$) Case SD: ○, 366; ⊙, 1272; □, 1962; ⊡, 3930; ▼, 19 947; ●, 30 920.

dissipation); see tables 1 and 2. Only during the very early phase ($21 < t/t_* < 37$) of Case VR does $\Delta x/\eta_{min}$ briefly exceed 5 (the nominal resolution threshold for DNS of non-wall-bounded turbulence; cf. Sandham 2002), but not by enough to suggest the present (fully spectral) discretization does not capture all relevant scales of motion.

A more direct test of the spatial (and temporal) resolution is provided by figure 3($b$), which presents histories of the lateral-area-integrated rate of change of the turbulence kinetic energy (open symbols) and the rate of net (production minus dissipation) resolved by the simulations (closed symbols), for both Cases VR (circles) and SD (squares). The good agreement between the two, indicated by the tendency for the closed symbols to overlie the open ones, over the course of both simulations, provides confidence in the numerical solutions presented below.

The final column in tables 1 and 2 shows the history of the local volume-flux defect $I_d$, which for this flow should remain constant; the very small deviation from the initial value $I_{do}$, even at very late times, is a further indication of the reliability of the DNS results.

https://doi.org/10.1017/jfm.2012.371 Published online by Cambridge University Press

| Symbol | Case VR $t/t_*$ | $U_d/U_{do}$ | $h/\rho_*$ | $U_d\,\delta_*/\nu$ | Case SD $t/t_*$ | $U_d/U_{do}$ | $h/\rho_*$ | $U_d\,\delta_*/\nu$ |
|---|---|---|---|---|---|---|---|---|
| | 0 | 1.0000 | 1.156 | 2171 | 0 | 1.0000 | 1.156 | 2171 |
| ♠ | 22 | 0.9991 | 1.162 | 2170 | 32 | 0.9951 | 1.152 | 2166 |
| ◇ | 29 | 0.9777 | 1.025 | 2147 | 40 | 0.8659 | 1.129 | 2020 |
| ♣ | 39 | 0.6909 | 1.038 | 1805 | | | | |
| ⊛ | 127 | 0.1917 | 1.089 | 951 | | | | |
| ⊞ | 219 | 0.1093 | 1.108 | 718 | | | | |
| ○ | 334 | 0.0706 | 1.118 | 577 | 366 | 0.0323 | 1.040 | 391 |
| △ | 708 | 0.0403 | 1.092 | 436 | 622 | 0.0247 | 1.011 | 342 |
| ▽ | 960 | 0.0335 | 1.049 | 397 | 936 | 0.0190 | 1.015 | 300 |
| ⊙ | 1299 | 0.0267 | 1.041 | 355 | 1272 | 0.0156 | 1.001 | 272 |
| □ | 2135 | 0.0170 | 1.045 | 283 | 1962 | 0.0117 | 1.012 | 236 |
| ◁ | 2832 | 0.0133 | 1.040 | 251 | 2544 | 0.0104 | 1.023 | 221 |
| ▷ | 3591 | 0.0111 | 1.082 | 229 | 3218 | 0.0091 | 1.021 | 208 |
| ⊡ | 4386 | 0.0093 | 1.098 | 210 | 3930 | 0.0082 | 1.008 | 197 |
| ▲ | 9308 | 0.0053 | 1.080 | 159 | 9437 | 0.0047 | 1.059 | 148 |
| ▼ | 20272 | 0.0036 | 1.028 | 130 | 19947 | 0.0029 | 1.069 | 118 |
| ● | 30964 | 0.0025 | 1.060 | 108 | 30920 | 0.0023 | 1.067 | 103 |

TABLE 3. Symbol convention and corresponding mean-flow results for times shown in figures 4–19. Wake half-width $h$ ranges from $h/h_o = 1$ at $t/t_* = 0$ to 18.4 at $t/t_* = 30\,964$ for Case VR, and to 19.4 at 30 920 for Case SD. Integral thickness $\delta_* = \rho_*/(2\ln 2)^{1/2}$ (as in JGG).

## 4. Results

A summary of the mean-flow characteristics for the various times considered in this paper, along with the symbols associated with each time, can be found in table 3.

### 4.1. *The non-universal self-similar regime*

The temporal development of the vortex-ring-initialized flow, Case VR, is illustrated by the vorticity contours in figure 5. The breakdown of the individual rings (figure 5*a*), which is triggered by the geometric perturbation described in § 3, and the rings' interaction with each other, quickly leads to a fully developed turbulent wake. As early as $t/t_* = 29$ (figure 5*b*), the turbulence structure shows no obvious trace of the vortex-ring initialization (see also spectra in figure 4*a*). The lateral spreading of vortical fluid into the initially irrotational background, associated with the growth of the wake width, is also apparent in figure 5, as is the increased lateral domain size needed to capture it.

The qualitatively different process by which Case SD becomes fully turbulent is revealed in figure 6. In contrast to Case VR's nonlinear/bypass transition, the broad-band low-amplitude initialization of Case SD triggers exponential growth and eventual breakdown of a linear helical-mode instability (figure 6*a*,*b*). Since it incorporates the entire transition process, the time required for Case SD to become fully turbulent is larger than it is for Case VR (highlighting the advantage of the latter's initialization scheme for making optimal use of finite computational resources when simulating fully turbulent wakes). But while both cases eventually become fully turbulent, their final states in this first time period (i.e. up to around $t/t_* = 1300$) are not equivalent, in terms of their large-scale structure and their interaction with the surrounding irrotational background. This can be seen from the vorticity contours in figures 5(*d*) and 6(*d*). Paradoxically, Case VR – born from a streamwise chain of discrete vortex

https://doi.org/10.1017/jfm.2012.371 Published online by Cambridge University Press

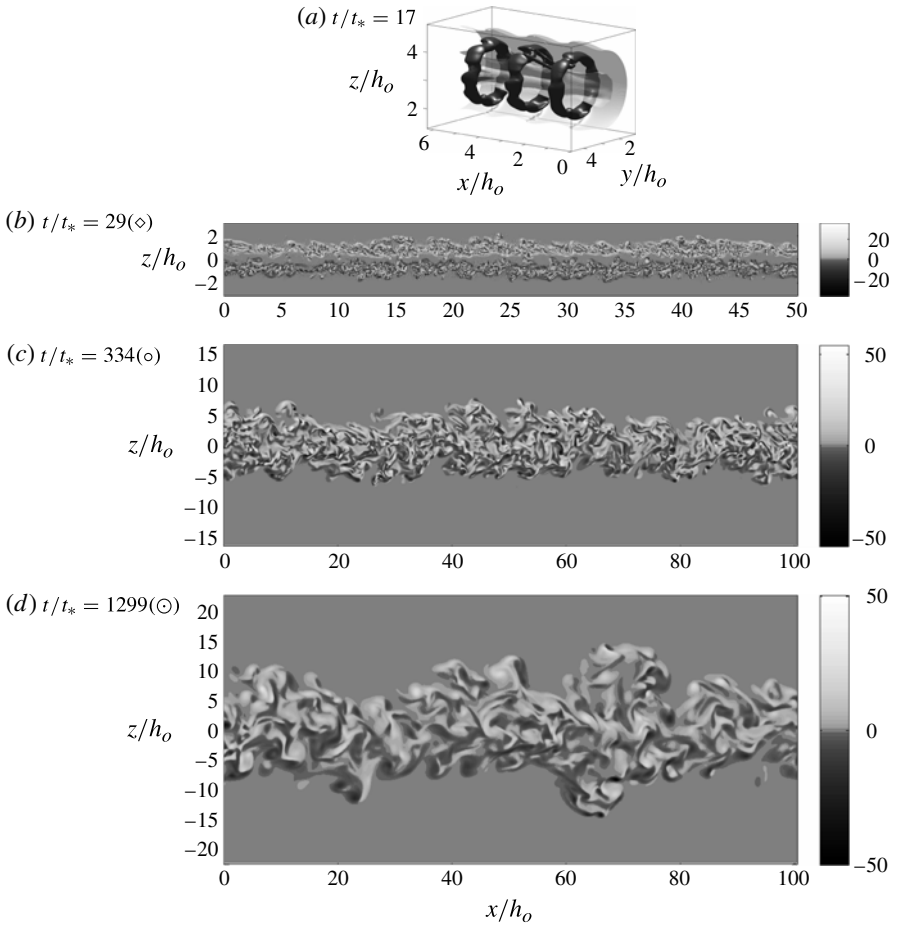


FIGURE 5. Instantaneous vorticity contours for Case VR at $t/t_* = 17, 29, 334, 1299$ for ($a$–$d$) respectively: ($a$) vorticity magnitude $|\omega|$ iso-surfaces, corresponding to 0.01 (light) and 1.0 (dark) of the local maximum of the axially averaged $|\omega|$ within the domain, and ($b$–$d$) vorticity component into the page in the vertical plane containing the wake centreline. Vorticity normalized with local $U_{max}$ and local wake width $L = 2h$. Axial flow in the free stream from right to left. Plots show the full lateral domain at each time, but only selected streamwise regions of the full $\Lambda_x = 64\pi h_o \approx 200 h_o$ domain. Symbols in labels correspond to times shown in figures 4 and 7–12 (see table 3).

rings (figure 1$a$) – exhibits a less varicose structure (i.e. with less streamwise 'clumpiness') than does Case SD, whose initial flow had essentially no streamwise variation (figure 1$b$).

The structural differences seen in figures 5 and 6 are quantified by the intermittency profiles $\gamma(r)$ in figure 7, which illustrate the fraction of vortical fluid at various radial locations across the wake. In this and other profiles to follow, the radial coordinate $r$ has been normalized by $\rho_*$, an integral length scale given by

$$\rho_*^2 = \frac{\ln 2}{\pi} \frac{I_d}{U_d}, \tag{4.1}$$

https://doi.org/10.1017/jfm.2012.371 Published online by Cambridge University Press

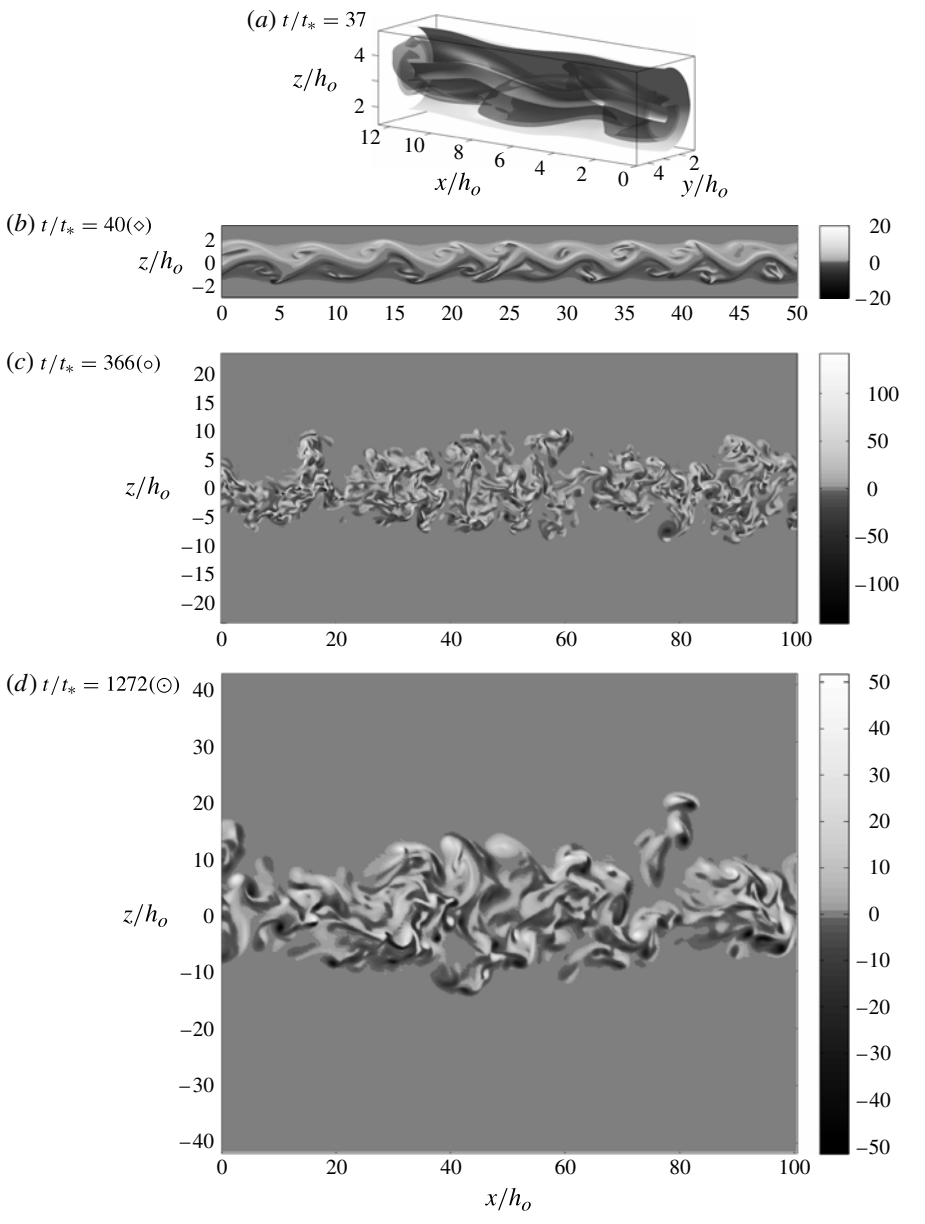


FIGURE 6. Instantaneous vorticity contours for Case SD at $t/t_* = 37, 40, 366, 1272$ for $(a–d)$ respectively: $(a)$ vorticity magnitude $|\omega|$ iso-surfaces, and $(b–d)$ vorticity component into the page in the vertical plane containing the wake centreline. See figure 5 caption for information regarding normalization and symbols shown in labels. Plots show the full lateral domain at each time, but only selected streamwise regions of the full $\Lambda_x = 128\pi h_o \approx 400 h_o$ domain.

defined so that $\rho_* = h$ for a Gaussian mean-velocity profile. This differs from the length scale $\delta_*$ used by JJG, with $\delta_* = \rho_*/(2 \ln 2)^{1/2}$. (For a Gaussian mean, $\delta_*$ is equivalent to the $L_c$ used by Bevilaqua & Lykoudis 1978.) For ease of comparison, $\delta_*$ will be used to define the mean wake Reynolds number $U_d \delta_* \nu$.

https://doi.org/10.1017/jfm.2012.371 Published online by Cambridge University Press

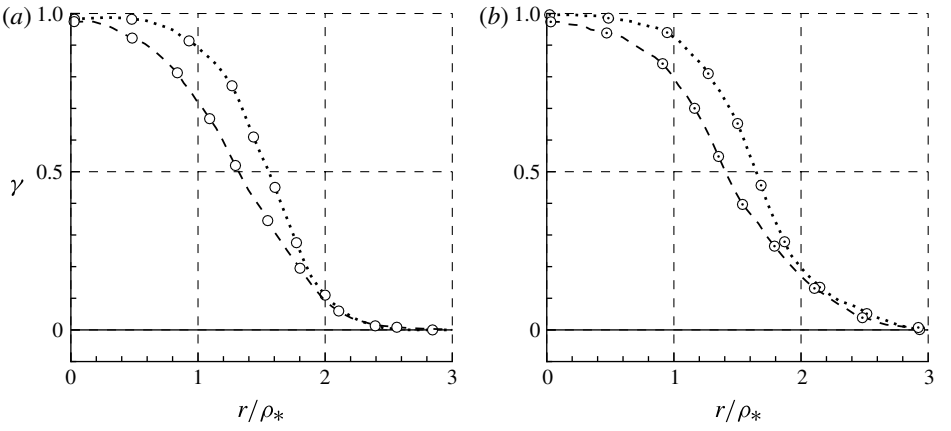


FIGURE 7. Intermittency profiles: ·····, Case VR; - - - -, Case SD. Symbols correspond to times shown in figures 10 and 11: (*a*) ○, $t/t_* = 334$ (VR) and 366 (SD); (*b*) ⊙, $t/t_* = 1299$ (VR) and 1272 (SD). The threshold between vortical and irrotational flow is defined as 0.01 of maximum local/instantaneous vorticity magnitude.

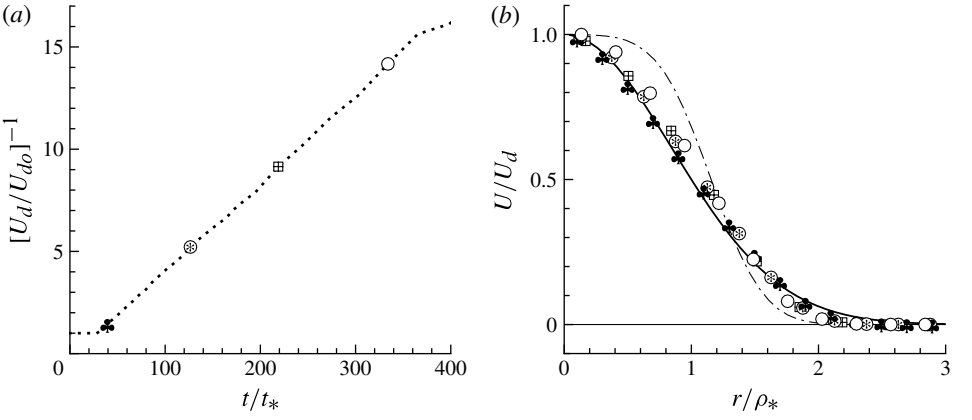


FIGURE 8. Early mean-flow evolution for Case VR: (*a*) similarity diagnostic for $U_d$ with $n = 1/2$. Symbols added in (*a*) indicate times for which mean profiles are shown in (*b*): $t/t_* =$: ♣, 39; ⊛, 127; ⊞, 219; ○, 334. – · –, Initial profile ($t = 0$); —, $U/U_d = \exp(-\ln(2)\,(r/\rho_*)^2)$.

The tendency for $\gamma$ to fall below unity at smaller $r$ for Case SD is evidence of the irrotational fluid near the centreline apparent in figure 6(*d*). However, a comparison of figures 7(*a*) and 7(*b*) (corresponding respectively to $t/t_* \approx 350$ and 1300, the last two times shown in figures 5 and 6), reveals that as time passes, the intermittency profile for Case SD (dashed line) approaches that for Case VR (dotted line) near the centreline.

We now turn to the question of self-similarity of the mean velocity. Surprisingly, the very early state of Case VR (when the Reynolds number is highest) clearly demonstrates $n = 1/2$ (low-Reynolds-number) behaviour. This is apparent from figure 8(*a*), which shows the early history of the mean centreline defect $U_d$. For all the results to follow, both the magnitude of $U_d$ and the location $y_0, z_0$ about

https://doi.org/10.1017/jfm.2012.371 Published online by Cambridge University Press

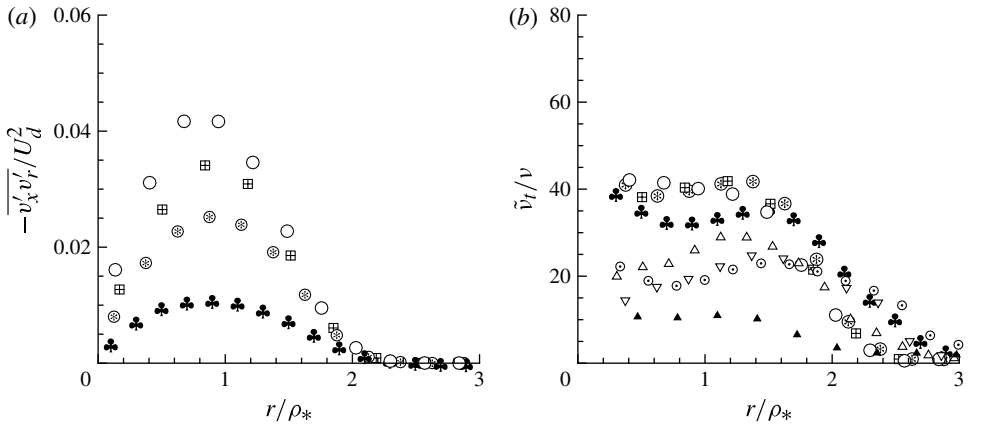


FIGURE 9. Early evolution of Case VR profiles of (*a*) shear-stress $\overline{v_x'v_r'}$ and (*b*) eddy-viscosity diagnosistic $\widetilde{\nu}_t = [-\overline{v_x'v_r'}/(\partial G/\partial r)]$, where $G$ is the Gaussian mean-velocity profile, such that $\partial G/\partial r = (2\ln 2\, U_d r/\rho_*^2)\exp(-\ln 2\,(r/\rho_*)^2)$, at $t/t_* =$: ♣, 39; ⊛, 127; ⊞, 219; ○, 334; △, 708 (in *b*); ▽, 960 (in *b*); ⊙, 1299 (in *b*); ▲, 9308 (in *b*).

which azimuthal averages have been taken were defined as the values at the centroid of the axially averaged mean velocity $\langle u\rangle$ at each time, with $y_0 = \int_y\int_z y\langle u\rangle \mathrm{d}y\,\mathrm{d}z/I_d$, where $I_d = \int_y\int_z\langle u\rangle \mathrm{d}y\,\mathrm{d}z$, and similarly for $z_0$. (Other approximations for $U_d$, such as the maximum $\langle u\rangle$ over the $y$–$z$ plane, or along horizontal or vertical cuts through the geometric centreline (used by Gourlay *et al.* and JGG), can, as we shall see, cloud interpretation of the data, especially at later times.) The linear variation of $U_d^{-1}$, combined with the close agreement between the mean profile and the Gaussian idealization near the centreline seen in figure 8(*b*), point to the presence of the $n = 1/2$ solution. Further evidence is given in figures 9(*a*) and 9(*b*), which respectively show profiles of the $-\overline{v_x'v_r'}$ shear stress and $\widetilde{\nu}_t$, a measure of the eddy viscosity. For the latter, the actual mean velocity gradient $\partial\overline{v}_x/\partial r$ from the DNS has been replaced by the analytic Gaussian profile, in order to minimize statistical uncertainty associated with this quantity. (Recall that determining $\nu_t$ involves averaging over a single finite-domain realization, then forming the ratio of one statistic and the derivative of another, both of which approach zero near the centreline.) The $\widetilde{\nu}_t$ data points closer to the axis than those shown are not included because of the inevitably much larger scatter there. Both the shear-stress and the eddy-viscosity diagnostic are consistent with the similarity analysis, which predicts $-\overline{v_x'v_r'}/U_d^2 \propto t^{3n-1}$ and $\nu_t/\nu \propto t^{2n-1}$, in that the former grows and the latter tends to remain fixed with time. Note also the magnitude of $\widetilde{\nu}_t$ and its approximately constant radial variation for $r < \rho_*$ (such that the core of the flow evolves as if it were laminar) for these times. Therefore, as pointed out in § 2, we find that $n = 1/2$ behaviour does not require $\nu_t$ and $\nu$ to be of the same order, provided temporal variations of $\nu_t$ are negligible. This in turn implies that the $n = 1/2$ solution is not necessarily associated with low Reynolds number, since here the uniformity and steadiness of $\nu_t$, rather than the magnitude of $Re$, causes the Reynolds-stress and viscous terms in (2.1) to share the same profile.

After $t/t_* = 334$, $\widetilde{\nu}_t/\nu$ begins to decrease with time, as Case VR enters the $n = 1/3$ regime. The linear variation of the $U_d^{-3/2}$ history shown in figure 10(*a*) (and the $U_d^{-1}$ history shown in figure 8*a*) suggests that the Case VR mean defect satisfies the

https://doi.org/10.1017/jfm.2012.371 Published online by Cambridge University Press

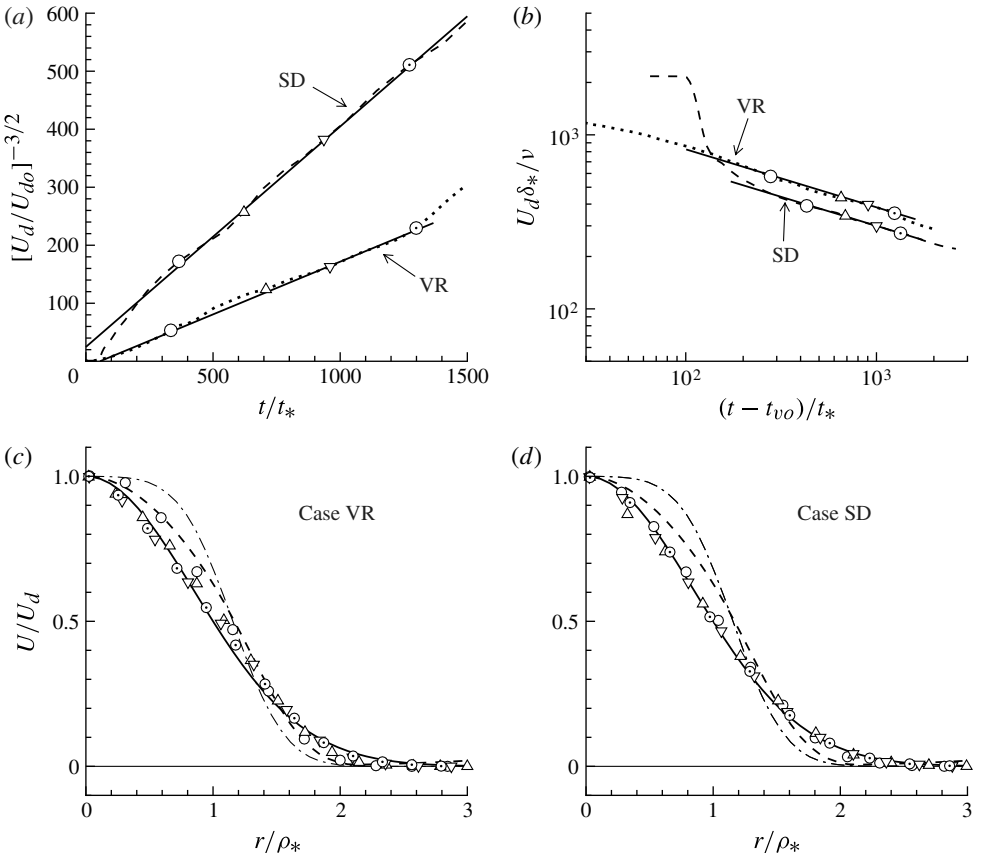


FIGURE 10. Mean-flow evolution for $t/t_* < 1300$. (*a*) Similarity diagnostic for $U_d$: ·····, Case VR; - - - -, Case SD; —, linear curve-fit $A\,(t/t_* - t_{vo}/t_*)$ with $(A, t_{vo}/t_*) = (0.18, 55.5)$ and $(0.38, -65)$ for Cases VR and SD, respectively. (*b*) Mean Reynolds number $U_d\,\delta_*/\nu$: ·····, Case VR; - - - -, Case SD; —, power-law $C\,(t/t_* - t_{vo}/t_*)^{-1/3}$ implied by curve-fit in (*a*), where $C = 3833$ (VR) and 3000 (SD), and $t_{vo}/t_*$ as in (*a*). Symbols in (*a*) and (*b*) indicate times for which mean profiles are shown in (*c*) and (*d*) (and elsewhere): (*c*) Case VR, $t/t_* =:$ ○, 334; △, 708; ▽, 960; ⊙, 1299. (*d*) Case SD, $t/t_* =:$ ○, 366; △, 622; ▽, 936; ⊙, 1272. – · –, Initial profile ($t = 0$); —, $U/U_d = \exp(-\ln(2)\,(r/\rho_*)^2)$; - - - -, JGG's equation (C7).

high-*Re* similarity condition (2.7) for $t/t_*$ greater than ∼300. Incidentally, although it is tempting to define an equivalent momentum thickness $\theta$ for the present time-dependent homogeneous wake, to allow a direct comparison with results from the spatially developing experiments (as JGG did), this cannot be done unambiguously, since it would involve the product of the volume-flux deficit $I_d$ and a free-stream velocity $V_\infty$ – which here can only be represented by an arbitrary Galilean reference velocity. (JGG appear to have assumed $V_\infty = U_{do}$.)

Figure 10(*c*,*d*) confirms that to a good approximation the entire mean profile is self-similar. For both flows, $U(\eta)/U_d$ is closer to the (uniform-$\nu_t$) Gaussian idealization (solid line) than the interpolant used by JGG for their $n = 1/3$ data (dashed line), especially at later times. The most significant message of figure 10(*a*) is that although the mean profiles from both wakes collapse to approximately the

https://doi.org/10.1017/jfm.2012.371 Published online by Cambridge University Press

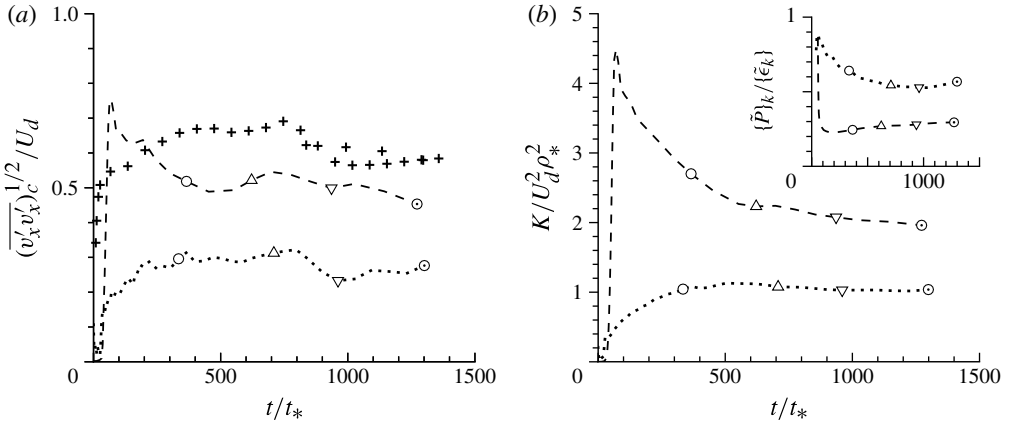


FIGURE 11. Histories of (*a*) root-mean-squared streamwise velocity fluctuation $v_x'$ at the centreline and (*b*) area-integrated turbulence kinetic energy $K = (1/2)\{\langle v_i' v_i' \rangle\}$: ·····, Case VR; - - - -, Case SD; + (in *a* only), Gourlay *et al.* (2001). Inset plot in (*b*) shows ratio of area-integrated rates of turbulence kinetic energy production $\{\widetilde{P}_k\}$ to dissipation $\{\widetilde{\epsilon}_k\}$ (see figure 3 for definitions). Symbols in (*a*) and (*b*) correspond to times for which Case VR and SD profiles are shown in other figures.

same $r/\rho_*$ variation, the $U_d^{-3/2}$ histories have very different slopes – and thus different growth rates – indicating their similarity is *not* universal. In other words, the Townsend coefficient $C_T$ in (2.7) is not constant, and thus the Townsend universal-behaviour hypothesis is not satisfied over the time period considered. (Since time has been normalized by the initial $\rho_*/U_d[= (\ln 2\, I_d/\pi U_{do}^3)^{1/2}]$, the slope of the $U_d^{-3/2}$ history is directly related to $C_T$.) The time-developing version of the non-dimensional mean spreading parameter $\beta = (\mathrm{d}h/\mathrm{d}t)/U_d$ can be calculated for both wakes using the linear interpolant in figure 10(*a*). Cases VR and SD respectively have $\beta \approx 0.06$ and $\beta \approx 0.13$, where we have used $\rho_*$ to estimate $h$. (Written in terms of the non-dimensional slope $A = \mathrm{d}\,(U_d/U_{do})^{-3/2}/\mathrm{d}(t/t_*)$, the mean spreading rate $\beta = (1/3)\,(\ln 2/\pi)^{1/2}\, A\, \zeta^{1/2}$ and the Townsend coefficient $C_T = A^{-2/3}\zeta^{-1/3}$, where, for both VR and SD, $\zeta = I_d/U_{do}\rho_{*o}^2 = 4.536$.) The Case SD wake thus spreads at about the same rate as the Gourlay *et al.* flow, for which $\beta \approx 0.15$. We therefore observe, following Bevilaqua & Lykoudis (1978) and JGG, that differences in turbulence structure introduced into the wake by the initialization (or body shape), can lead to long-lasting non-universal behaviour. However, we emphasize that this non-universal, though self-similar behaviour does not continue indefinitely, as will be shown in § 4.2.

The differences between the two cases in this non-universal period are even more pronounced in the second-order statistics. Although involving the more gentle (low-level, linear-disturbance) perturbation, the SD initialization eventually produces turbulence with not only a larger rate of spreading and more large-scale intermittency (figure 7), but also with kinetic energy that is a larger fraction of the mean defect $U_d$. Contrast the dotted and dashed lines in figures 11(*a*) and 11(*b*), which respectively illustrate histories of $(\overline{v_x'v_x'})_c^{1/2}/U_d$, the root-mean-squared streamwise velocity fluctuations at the wake centreline $y_0, z_0$ (as defined above), and the area-integrated turbulence kinetic energy. On the other hand, the net rate of (area-integrated) production of turbulence kinetic energy is a smaller fraction of its rate of dissipation

https://doi.org/10.1017/jfm.2012.371 Published online by Cambridge University Press

for Case SD (see figure 11*b* inset). The other results (crosses) in figure 11(*a*) are from Gourlay *et al.*'s time-developing axisymmetric-wake DNS, which was initialized with large-amplitude disturbances superimposed on a Gaussian mean profile. The Gourlay results were obtained by finding the maximum (rather than the centreline) streamwise-mean of the streamwise velocity fluctuations along horizontal and vertical lines (in the lateral plane) through the geometric centre of their domain, and normalizing by the corresponding horizontal- or vertical-line maximum streamwise-mean velocity (hence the two separate traces in their paper, evident particularly at later times; see figure 16*a* below). Computing the same two quantities for Cases VR and SD showed that the plane-maximum ratio is consistently about 15–20 % larger than the $(\overline{v_x' v_x'})_c^{1/2}/U_d$ defined here, which suggests that for the period considered the energy levels for the Gourlay *et al.* flow and Case SD are quite similar. The distinct strategies used to initialize the Gourlay *et al.* and Case SD simulations (finite and infinitesimal random disturbances, respectively, added to Gaussian and vortex-ring-induced means) thus both lead to comparable states, in terms of the magnitudes, relative to $U_d$, of the streamwise velocity fluctuations.

Comparing the evolution of the Reynolds-stress and $U_d$ profiles confirms Tennekes & Lumley's (1972) observation that the mean flow becomes self-similar before the second-order statistics do. While the $t/t_* \approx 350$ profiles of $U(\eta)/U_d$ are fairly close to those at $t/t_* \approx 1300$ for both cases (figure 10*c*,*d*), the same cannot be said about $-\overline{v_x' v_r'}/U_d^2$ (figure 12*a*,*b*): note the difference between the $t/t_* \approx 350$ (open circles) and $t/t_* \approx 1300$ (dotted circles) results, which is especially pronounced for Case SD at larger $r/\rho_*$ (where the azimuthal average is more certain and the contribution to the area integral is greater). This large difference is reflected in the persistent downward drift with time of the Case SD area-integrated kinetic energy seen in figure 11(*b*).

Using the scaling defined by the second proportionality in (2.6), which shows that mean-flow universality requires $-\overline{v_x' v_r'} \propto \beta U_d^2$ (JGG), leads to the results presented in figure 12(*c*,*d*). The reasonably good agreement between the two flows is consistent with the tendency for the shape of the Case VR and SD mean profiles to be the same (figure 10*c*,*d*).

The $U$ and $-\overline{v_x' v_r'}$ profiles have been used to compute the viscous $T_v$ and turbulence $T_t$ contributions to the right-hand-side of the RANS equation (2.1), the sum of which, $T_s$, is plotted with the similarity scaling in figure 12(*e*,*f*). Also shown, as the solid-diamond symbol at $r = 0$, is $\mathrm{d}U_d/\mathrm{d}t$ defined by the two $U_d$ curve-fits from figure 10(*a*). In view of the increased uncertainty as $r \to 0$ of azimuthally averaged quantities, the compatibility, for both flows, of the $r = 0$ value with the $r > 0$ portion of the $T_v + T_t$ profile is encouraging.

The relatively insignificant contribution the viscous term makes to the RANS balance during this phase of the wake development is clear (compare, in figure 12*e*,*f*, the small and large dotted-circle symbols, which respectively correspond to the viscous and total (viscous plus turbulence) terms at $t/t_* \approx 1300$). High-*Re* $n = 1/3$ behaviour is observed here even though $U_d\,\delta_*/\nu$ becomes significantly smaller than 500, the threshold below which JGG propose $n = 1/2$ evolution will be found. Near $t/t_* = 1300$, it is roughly 350 and 270, for Cases VR and SD respectively (figure 10*b* and table 3). We shall see below that $n = 1/3$ behaviour persists at even smaller *Re*, as low as $U_d\,\delta_*/\nu \approx 100$. Using the disappearance of a $\kappa^{-5/3}$ region in the spectrum as the criterion for the critical Reynolds number (as JGG did) is apparently not appropriate.

https://doi.org/10.1017/jfm.2012.371 Published online by Cambridge University Press

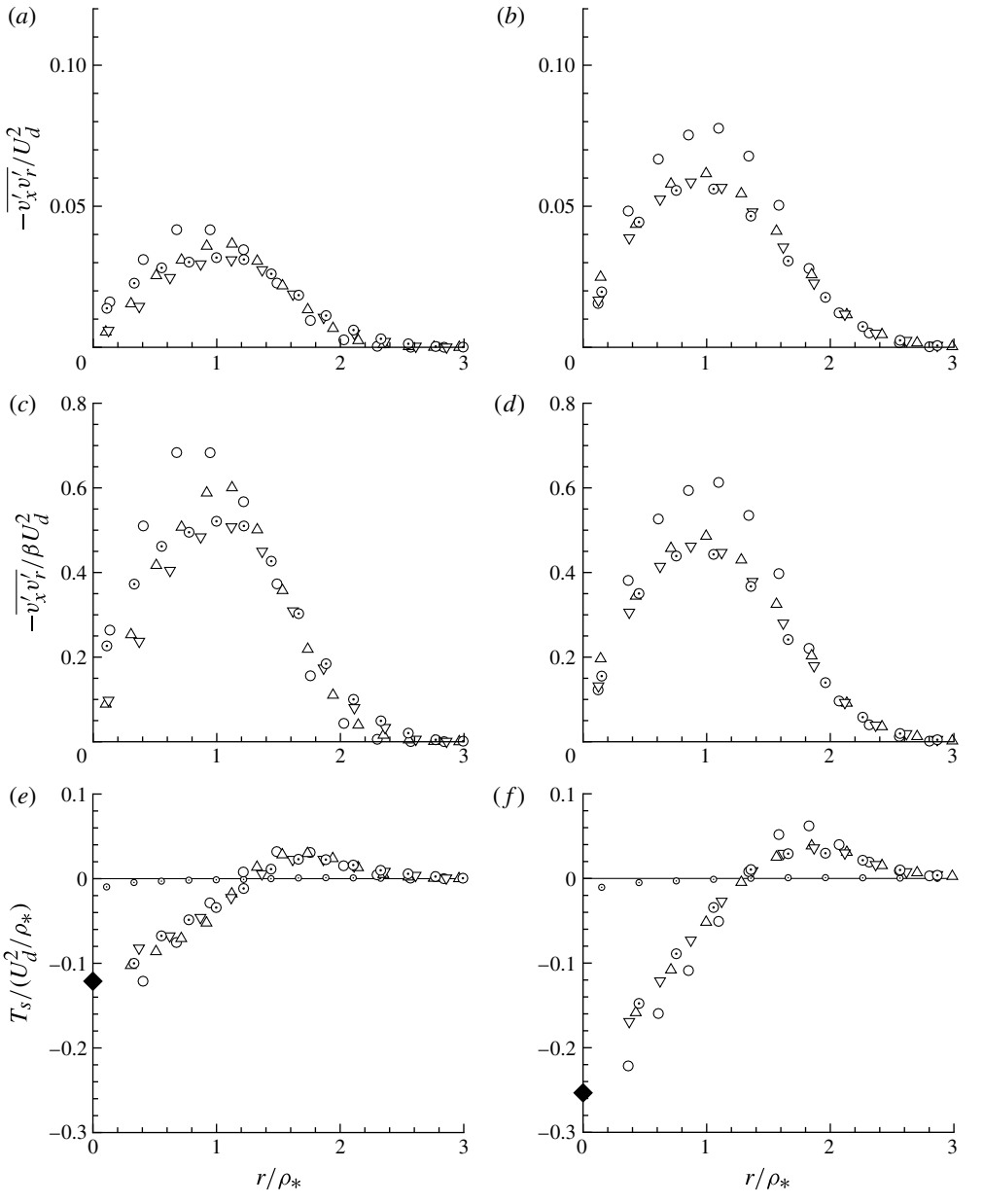


FIGURE 12. Profiles of shear stress and terms in the RANS equation: (*a*,*c*,*e*) Case VR, $t/t_* =$: ○, 334; △, 708; ▽, 960; ⊙, 1299. (*b*,*d*,*f*) Case SD, $t/t_* =$: ○, 366; △, 622; ▽, 936; ⊙, 1272. In (*e*) and (*f*), the large symbols indicate $T_s$, the sum of the Reynold-stress $T_t$ and viscous $T_v$ terms in the RANS equation, where $T_t = -(1/r)\partial(r\,\overline{v_x' v_r'})/\partial r$ and $T_v = (1/r)\partial(r\,\nu\,\partial\overline{v}_x/\partial r)/\partial r$, while the smaller symbols (⊙) show $T_v$ at $t/t_* = 1299$ (VR) and $t/t_* = 1272$ (SD), and the larger symbol (♦) at $r = 0$ is $\mathrm{d}U_d/\mathrm{d}t$ from a linear curve-fit of the $U_d^{-3/2}$ history shown in figure 10(*a*), which implies $\mathrm{d}U_d/\mathrm{d}t = -(2A/3)\,U_d^2/\rho_*$, with $A = 0.18$ for Case VR and 0.38 for Case SD.

https://doi.org/10.1017/jfm.2012.371 Published online by Cambridge University Press

The Case VR wake ($\beta \approx 0.06$) is analogous to that downstream of Cannon & Champagne (1991)'s disk-shaped screen with 49 % blockage (for which $\beta = 0.064$ and $(\overline{v_x' v_x'})_c^{1/2}/U_d = 0.3$). The SD and Gourlay *et al.* flows, on the other hand, are characterized by spreading rates ($\beta \approx 0.15$) and centreline fluctuations ($(\overline{v_x' v_x'})^{1/2}/U_d \approx 0.6$) lying between those found in wakes generated by e.g. Chevray's (1968) 6:1 ellipsoid ($\beta \approx 0.1$, $(\overline{v_x' v_x'})^{1/2}/U_d \approx 0.3$), and by Cannon & Champagne's less porous (84 % blockage) disk ($\beta \approx 0.3$, $(\overline{v_x' v_x'})^{1/2}/U_d \approx 0.75$); see Pope (2000).

Before considering the wake evolution at very long times, we attempt to place the present results in context by determining the effective downstream distance associated with the time period considered thus far. A standard control-volume analysis of the incompressible spatially developing wake far downstream of a spherical body of diameter $d$ immersed in a fluid stream of density $\rho$ and speed $V_\infty$ gives $C_D \approx 8I_d/\pi V_\infty d^2$, where $C_D = F_D/(\pi\rho V_\infty^2 d^2/8)$ and $F_D$ is the drag force experienced by the body. In terms of the initial variables for the time-developing problem, we have $V_\infty/U_{do} = (2/\pi C_D)(2h_o/d)^2(\rho_{*o}/h_o)^2\zeta$, where $\zeta = I_d/U_{do}\rho_{*o}^2$. The effective downstream distance $x = V_\infty t$ can thus be written

$$\frac{x}{d} = \frac{\zeta}{\pi C_D}\left(\frac{2h_o}{d}\right)^3\left(\frac{\rho_{*o}}{h_o}\right)^3\left(\frac{t}{t_*}\right). \tag{4.2}$$

If we equate the virtual-body radius $d/2$ to the initial half-width $h_o$ of the time-developing flow (cf. figure 2 of Bevilaqua & Lykoudis 1978), and assume, say, $C_D = 0.4$, then (since $\zeta = 4.536$ and $h_o/\rho_{*o} = 1.156$) the latest (self-similar but non-universal) Cases VR and SD results, at $t/t_* \approx 1300$, correspond to a downstream distance $x/d \approx 3000$. For a 2.5 cm diameter body, this implies $x = O(75\,\mathrm{m})$ (!), which demonstrates the long-lasting nature of the initial-condition dependence found here (contrast Bevilaqua & Lykoudis's 1978 experiments, for which maximum $x/d = 120$).

### 4.2. *The universal self-similar regime*

The question to be addressed in this section is whether or not the initial-condition dependence, which yields the self-similar but non-universal behaviour explored in the previous section, lasts as long as the wake does (i.e. during the entire period before $\nu_t \to \nu$), or if instead the turbulence structure eventually becomes universal, such that Townsend's hypothesis is satisfied.

The late-time vorticity contours in figure 13 tend to support the latter option, in that the qualitative differences between Cases VR and SD are much less obvious than they were at earlier times (compare with figures 5*d* and 6*d*). This is quantified by the temporal development of the intermittency profiles $\gamma(r)$ in figure 14. The radial spread with time of the region of agreement between $\gamma$ for Cases VR (dotted lines) and SD (dashed) is striking. Figure 14(*d*) indicates that at the latest time, the fraction of vortical flow is identical for $r \leqslant \rho_*$.

This move towards increasing structural similarity is accompanied by a period of universal mean-flow development. The collapse of the mean velocity to identical similarity profiles (figure 15*c*,*d*) is no surprise, since, as shown by JGG, the mean-flow similarity variable $f(\eta)$ is unaffected by the structure of the wake turbulence. (Note the reasonable agreement with the Gaussian profile, which is again somewhat better than that for the JGG interpolant.) What could not be anticipated is the presence of identical slopes for the two $U_d$-similarity diagnostics in figure 15(*a*), which corresponds to identical mean spreading rates for Cases VR and SD, with $\beta \approx 0.10$, and thus equivalent values of the Townsend coefficient in (2.7), with $C_T \approx 1.35$.

https://doi.org/10.1017/jfm.2012.371 Published online by Cambridge University Press

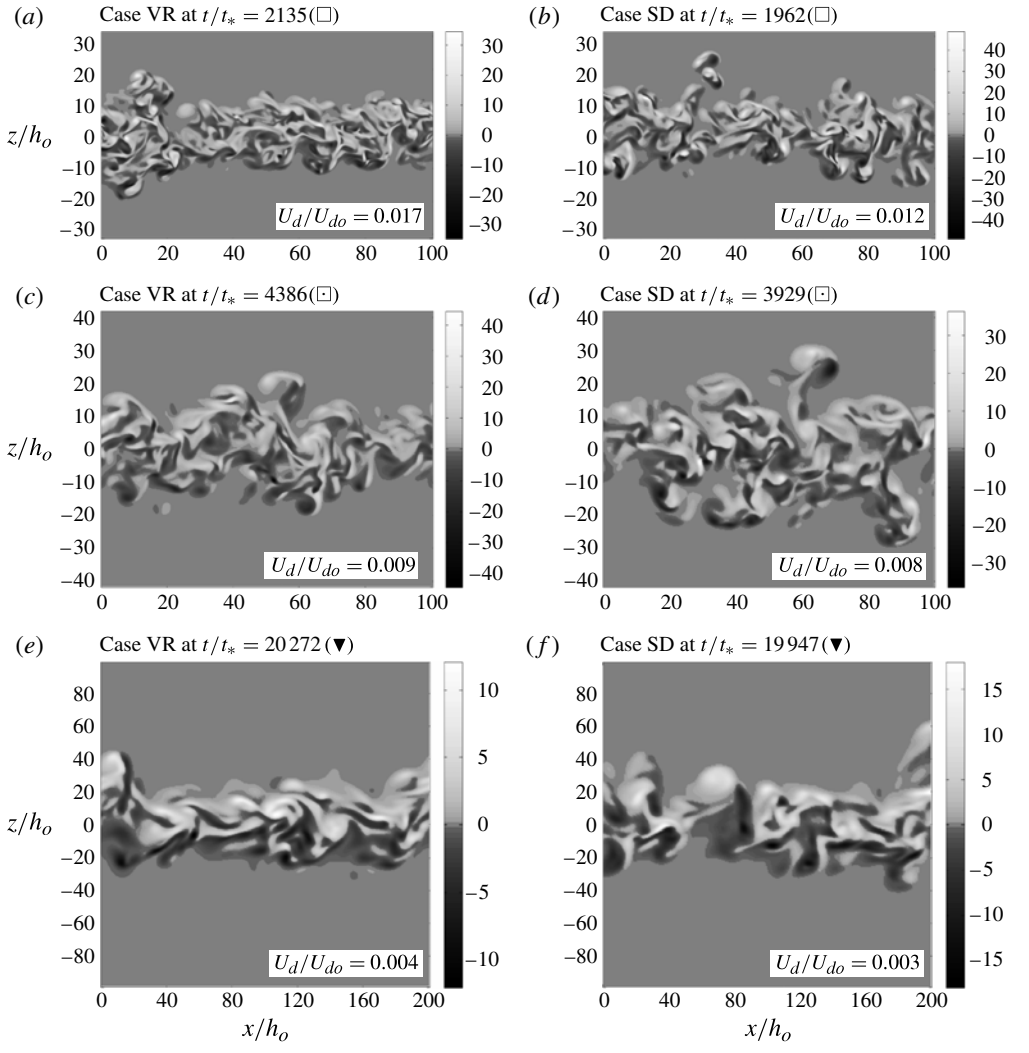


FIGURE 13. Vorticity contours for Case VR at $t/t_* =$: (*a*) 2135 (□); (*c*) 4386 (⊡); (*e*) 20 272 (▼); and Case SD at $t/t_* =$: (*b*) 1962 (□); (*d*) 3930 (⊡); (*f*) 19 947 (▼). Vorticity component shown is into the page in the vertical plane containing the wake centreline, normalized with respect to local $U_{max}$ and $\ell = 2h$. Axial flow is from right to left. For Case VR, regions shown correspond to the full lateral domain $\Lambda_z$ and either (*a*,*c*) one half or (*e*) the full streamwise domain $\Lambda_x$. To aid visualization, Case SD plots (*b*,*d*,*f*) show subregions of $\Lambda_z$ equivalent to Case VR's $\Lambda_z$ at a comparable time (see table 2), while the streamwise extent is either (*b*,*d*) one quarter or (*f*) one half of $\Lambda_x$. Symbols in labels coincide with times shown in figures 15–19 (see table 3).

It may at first glance appear that the agreement of $\beta$ for Cases VR and SD seen in figure 15(*a*), and thus the late-time universal behaviour, is an unphysical numerical artefact of the wake turbulence beginning to 'outgrow' the fixed streamwise domain. (See § 3 for discussion of the sufficiency of the size of the lateral domain.) The relative magnitude of the streamwise integral scale $\mathscr{L}_x$ (defined as the minimum-separation zero-crossing of the streamwise two-point correlation

https://doi.org/10.1017/jfm.2012.371 Published online by Cambridge University Press

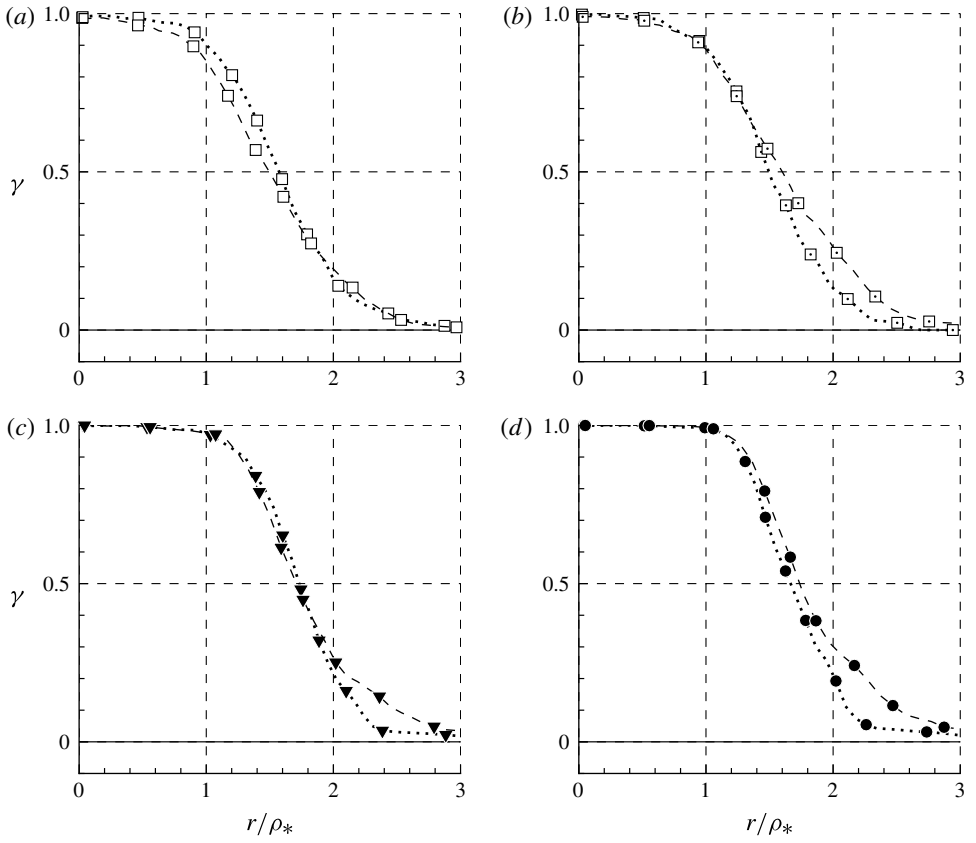


FIGURE 14. Intermittency profiles: ·····, Case VR; - - - -, Case SD. Symbols correspond to times shown in figures 15 and 16 (and elsewhere): (*a*) □, $t/t_* = 2135$ (VR) and 1962 (SD); (*b*) ⊡, $t/t_* = 4386$ (VR) and 3930 (SD); (*c*) ▼, $t/t_* = 20\,272$ (VR) and 19 947 (SD); (*d*) ●, $t/t_* = 30\,964$ (VR) and 30 920 (SD). The threshold between vortical and irrotational flow is defined as 0.01 of the maximum local/instantaneous vorticity magnitude.

$\overline{v_x'(x)v_x'(x+r_x)}/\overline{v_x'(x)v_x'(x)}$), suggests this is not the case, since for Cases VR and SD it remains, respectively, less than 6 % and 3 % of $\Lambda_x$ for $t/t_*$ less than about 4000 (corresponding to the dotted squares in figure 15*a*); even at the end of the simulations, near $t/t_* \approx 31\,000$ (solid circles), the domain remains large enough that $\mathscr{L}_x/\Lambda_x \approx 12\,\%$ for VR and 6 % for SD. Another argument follows simply from the $U_d(t)$ evolution observed in the universal regime, in that $t^{-2/3}$ behaviour is incompatible with dependence on an externally imposed length scale. (If $U_d$ were to depend on $\Lambda_x$ in addition to $I_d$ and $t$, (2.7) would be altered such that $C_T$ is replaced by a function of $\Lambda/\left(I_d(t-t_{vo})\right)^{1/3}$, implying $U_d$ would not scale with $t^{-2/3}$ if $\Lambda_x$ were to affect the spreading rate.) And finally, that the same $\beta$ appears at about the same time in domains whose $\Lambda_x$ differ by a factor of two also argues against any spurious numerical influence.

The universal growth rate defined by the linear interpolant in figure 15(*a*) is extended to later times in figure 15(*b*), and compared to the DNS. Also shown is the history of the ratio of the maximum $U_{max}$ to the centroid $U_d$ values of the axially averaged mean velocity $\langle u \rangle$ over the lateral $y$,$z$ plane. This ratio is always greater

https://doi.org/10.1017/jfm.2012.371 Published online by Cambridge University Press

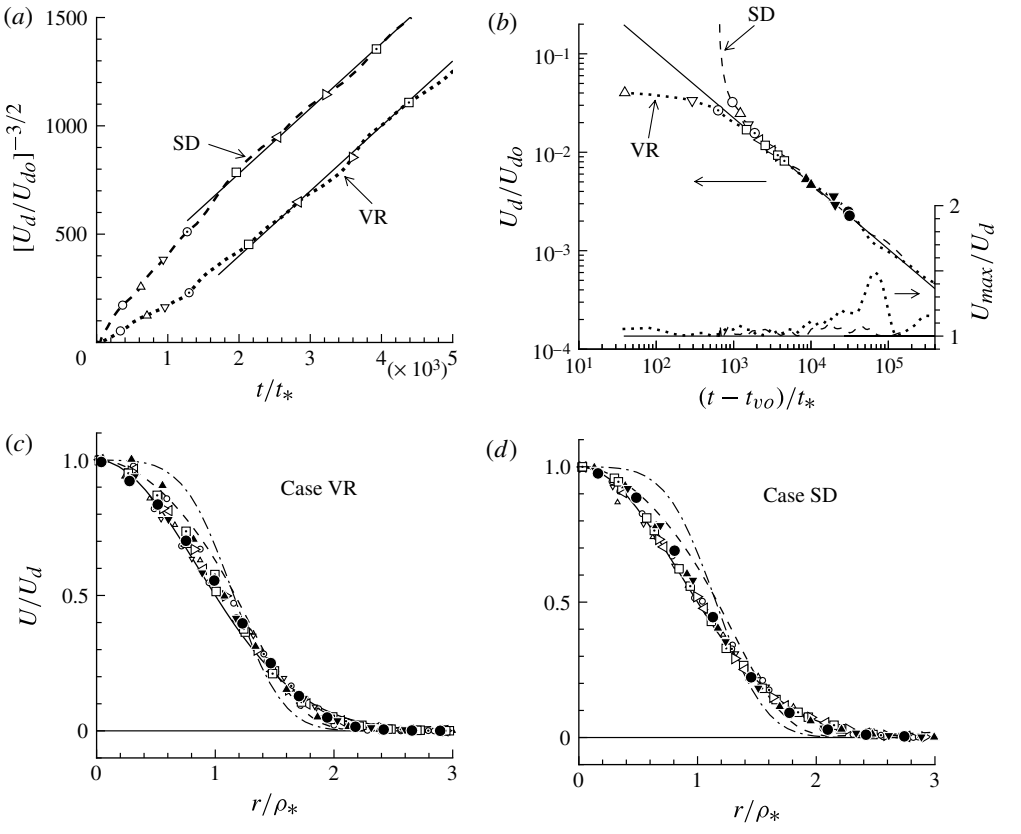


FIGURE 15. Mean-flow evolution including $t/t_* > 1300$: (*a*) Similarity diagnostic for $U_d$: ·····, Case VR; - - - -, Case SD; —, linear curve-fit $A\,(t/t_* - t_{vo}/t_*)$ with $A = 0.30$ and $t_{vo}/t_* = +670$ and $-600$ for Cases VR and SD, respectively. (*b*) Mean defect $U_d$: ·····, Case VR; - - - -, Case SD; —, power-law $U_d/U_{do} = B\,(t/t_* - t_{vo}/t_*)^{-2/3}$ implied by curve-fit in (*a*), where $B = 2.23$ and $t_{vo}/t_*$ as in (*a*). Symbols in (*a*,*b*) indicate times for which mean profiles are shown in (*c*) and (*d*) (and elsewhere): (*c*) Case VR, $t/t_* =$: ⊙, 1299; □, 2135; ◁, 2832; ▷, 3591; ⊡, 4386; ▲, 9308; ▼, 20 272; ●, 30 964. (*d*) Case SD, $t/t_* =$: ⊙, 1272; □, 1962; ◁, 2544; ▷, 3218; ⊡, 3930; ▲, 9437; ▼, 19 947; ●, 30 920; – · –, initial profile ($t = 0$); —, $U/U_d = \exp(-\ln(2)\,(r/\rho_*)^2)$; - - - -, JGG's equation (C7).

than or equal to unity, and its closeness to unity can be interpreted as a measure of the statistical reliability of the $U_d$ history. We observe that $U_{max}/U_d$ tends to drift upwards with time, and is consistently smaller (and therefore infer that its statistics are more accurate) for Case SD than for VR – a symptom of the larger averaging sample afforded by Case SD's larger $\Lambda_x$.

The agreement with the universal interpolant (solid line in figure 15*b*) is good for both wakes, for times before $U_{max}/U_d$ (and thus the statistical uncertainty) becomes large. The present findings therefore imply that the wake turbulence eventually reaches the universal state predicted by Townsend's hypothesis. The major collective evidences for this are, first, the $t^{-2/3}$ mean velocity behaviour and, second, the similarity of the turbulence structure – hinted at by the vorticity contour plots and quantified by the intermittency profiles. The agreement of the second-order statistics for Cases VR and SD, presented below, also points strongly to universality.

https://doi.org/10.1017/jfm.2012.371 Published online by Cambridge University Press

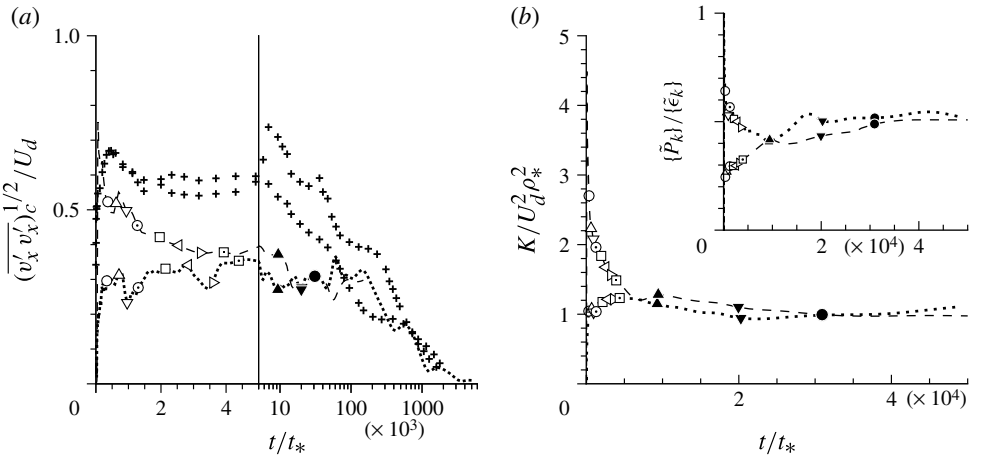


FIGURE 16. Histories of (*a*) root-mean-squared streamwise velocity fluctuation $v_x'$ at the centreline and (*b*) area-integrated turbulence kinetic energy $K = (1/2)\{\langle v_i' v_i' \rangle\}$ and (inset) ratio of area-integrated rates of production $\{\widetilde{P}_k\}$ and dissipation $\{\widetilde{\epsilon}_k\}$ (see figure 3 for definitions): ·····, Case VR; - - - -, Case SD. The + symbols in (*a*) are data from Gourlay *et al.* (2001), with their different definition of $v_x'$ and $U_d$ (see text). The other symbols in (*a*) and (*b*) correspond to times for which Cases VR and SD profiles are shown in other figures (see table 3).

However, the time required for the universal similarity to appear is large enough to imply that it will rarely if ever appear in flows of practical interest (except for the special case in which the flow's initial structure were to closely coincide with that associated with the universal state). Using (4.2) and the previous assumptions about a virtual body (i.e. $C_D \approx 0.4$, $d \approx 2h_o$), we find that the earliest indication of the universal $t^{-2/3}$ regime (at $t/t_* \approx 2000$) corresponds to a downstream distance of $x/d \approx 4700$! (Note the dotted circles in figure 15*a*, from $t/t_* \approx 1300$, near the end of the non-universal self-similar regime discussed earlier.) In other words, of the order of the first 100 m of a wake generated by a 2.5 cm diameter sphere would not exhibit universal behaviour.

Nevertheless, despite its possible absence in real-world flows, the universal regime seen here does possess some noteworth characteristics. One is the persistence of the high-*Re*, $n = 1/3$, behaviour, even though $U_d\,\delta_*/\nu$ is quite small for both VR and SD: at $t/t_* \approx 31\,000$ it is approximately 100 (table 3) – much less than the threshold of 500, below which JGG proposed $n = 1/2$ should be found. The continuing dominance, for the times examined here, of the turbulence term over the viscous term in the RANS equation will be illustrated below.

The Case SD histories of centreline streamwise-velocity fluctuation $v_x'$ and lateral-area-integrated turbulence kinetic energy in figure 16(*a*,*b*) (dashed lines) reveal the extent to which these quantities can deviate from non-self-similar behaviour without affecting the self-similarity of the mean flow. Examined over a longer time, the significant downward drift, in units of $U_d(t)$ and $\rho_*(t)$, of $|v_x'|$ and especially $K$ during its early $\beta \approx 0.13$ period (between $t/t_* \approx 300$ and 1300, corresponding respectively to the open and dotted circles in figure 16*a*,*b*) is more apparent than when the period is limited to the $0 \leqslant t/t_* \leqslant 1300$ range shown in figure 11. The relative speeds with which the $v_x'$ magnitudes become a fixed ratio of $U_d$ also suggest that the Case VR

https://doi.org/10.1017/jfm.2012.371 Published online by Cambridge University Press

initialization leads more quickly to a flow with (non-universal) self-similar normal Reynolds stresses than do Case SD's low-level random disturbances or Gourlay *et al.*'s finite-amplitude perturbations of a Gaussian mean.

The figure 16 histories demonstrate that the second-order statistics require much more time to become universal than the mean flow does. While the universal $\beta$ appears near $t/t_* = 2000$, the normal stresses do not become the same fraction of $U_d^2$ until after $t/t_* \approx 10\,000$ (solid symbols in figure 16); the area-integrated production-to-dissipation ratio $\{\widetilde{P}_k\}/\{\widetilde{\epsilon}_k\}$ arguably takes even longer (figure 16*b* inset).

In terms of the centreline turbulence intensity ($|v_x'|/U_d \approx 0.3$) and mean spreading rate ($\beta \approx 0.10$), full (second-order) universal self-similarity roughly corresponds to the wake downstream of the 6:1 ellipsoid (for which $(\overline{v_x' v_x'})^{1/2}/U_d = 0.3$ and $\beta = 0.11$), studied by Chevray (1968). Figure 16(*b*) shows that for the universal state, the area-integrated (axially averaged) turbulence kinetic energy $K$ is roughly $1.0 U_d^2 \rho_*^2$, and $\{\widetilde{P}_k\}/\{\widetilde{\epsilon}_k\}$ about 0.5. The latter implies that the wake turbulence is still far from the state of homogeneous-isotropic decay, for which $\{\widetilde{P}_k\}/\{\widetilde{\epsilon}_k\} \equiv 0$.

To confirm the expectation that the wake simulation will eventually become laminar, as the turbulence structures outgrow the streamwise domain, Case VR was continued until $t/t_* > 5 \times 10^6$. The eventual laminarization of the Case VR flow, characterized by $|v_x'|/U_d \to 0$ for $t/t_* > 10^6$, is apparent from figure 16(*a*) (dotted curve). We stress that this behaviour, which is also seen in the Gourlay *et al.* DNS, is a purely numerical phenomenon, due to the largest scales of the wake turbulence becoming too large for the (fixed) streamwise size of the DNS domain. (Analogous behaviour has been seen in the plane-channel DNS of Jiménez & Moin (1991), who also found that turbulence cannot survive when a periodic dimension of the domain is smaller than some critical value.)

The normal Reynolds-stress profiles are given in figure 17, for times spanning their full $n = 1/3$ period beginning from the start of the non-universal self-similar regime, $t/t_* \approx 350$. These show that for Case VR, the velocity fluctuations induced by the vortex-ring initialization (chain-dotted lines) quickly mature such that their magnitude, in terms of local $U_d$, and self-similar radial shape, are essentially invariant over the entire evolution of this flow, with perhaps a slight tendency to decrease with time upon entering the period of full (second-order) universality (a finding anticipated by the relatively flat centreline and area-integrated velocity-fluctuation histories in figure 16). This quasi-equilibrium between the mean flow and the turbulence energy exists despite the significant change of mean spreading rate $\beta$ experienced by Case VR (figure 15*a*). For Case SD, the velocity-fluctuation magnitude relative to $U_d$ decreases monotonically. Evidently, the Case SD transition process produces 'extra' kinetic energy that does not immediately impact on the evolution of the mean flow.

While changes of the normal stresses only affect the mean flow to the extent that they influence the $-\overline{v_x' v_r'}$ component, changes of the latter are directly linked to the mean-flow evolution through the RANS equation (2.1). The convergence towards a universal $-\overline{v_x' v_r'}$ profile for Cases VR and SD observed in figure 18(*a*,*b*) is thus a necessary and sufficient condition for the convergence of the mean spreading rates $\beta$ seen in figure 15(*a*). The corresponding convergence of the profile of net $\partial U/\partial t$, given by the sum $T_s$ of the viscous $T_v$ plus turbulence $T_t$ RANS terms, is shown in figure 18(*c*,*d*). The move towards universality involves a gradual increase with time of $|T_s|/(U_d^2/\rho_*)$ for Case VR, and a more rapid decrease for Case SD, such that for both cases the net $\partial U/\partial t$ profile near the centreline is consistent with the (identical) $\mathrm{d}U_d/\mathrm{d}t$ defined by the two $U_d$ histories (solid diamond).

https://doi.org/10.1017/jfm.2012.371 Published online by Cambridge University Press

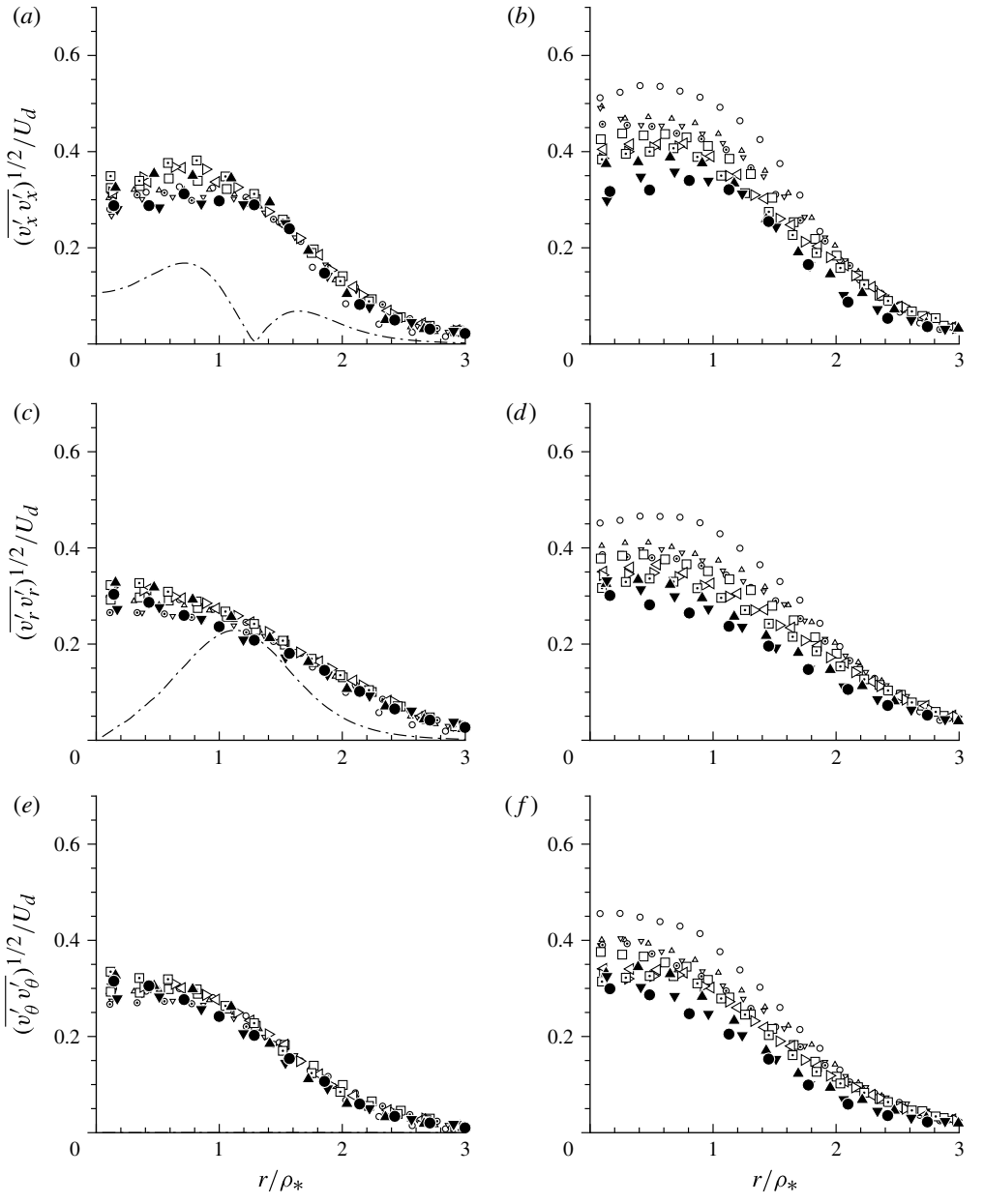


FIGURE 17. Velocity fluctuation profiles: – · –, initial profile, $t = 0$ (negligible in (*b*,*d*,*e*,*f*)); (*a*,*c*,*e*) Case VR, $t/t_* =$: ○, 334; △, 708; ▽, 960; ⊙, 1299; □, 2135; ◁, 2832; ▷, 3591; ⊡, 4386; ▲, 9308; ▼, 20 272; ●, 30 964. (*b*,*d*,*f*) Case SD, $t/t_* =$: ○, 366; △, 622; ▽, 936; ⊙, 1272; □, 1962; ◁, 2544; ▷, 3218; ⊡, 3930; ▲, 9437; ▼, 19 947; ●, 30 920.

The smallest (solid) symbols in figure 18(*c*,*d*) illustrate the contribution of the viscous term to the total RANS balance at the latest time shown. Its relatively small size (of order 1/10 of $T_t$) is at first glance rather surprising, given the magnitude of the mean centreline defect ($U_d/U_{do} \approx 0.002$), the smallness of the Reynolds number ($U_d\,\delta_*/\nu \approx 100$) and the deviation from $\kappa^{-5/3}$ inertial-subrange behaviour (figure 4*c*,*d*)

https://doi.org/10.1017/jfm.2012.371 Published online by Cambridge University Press

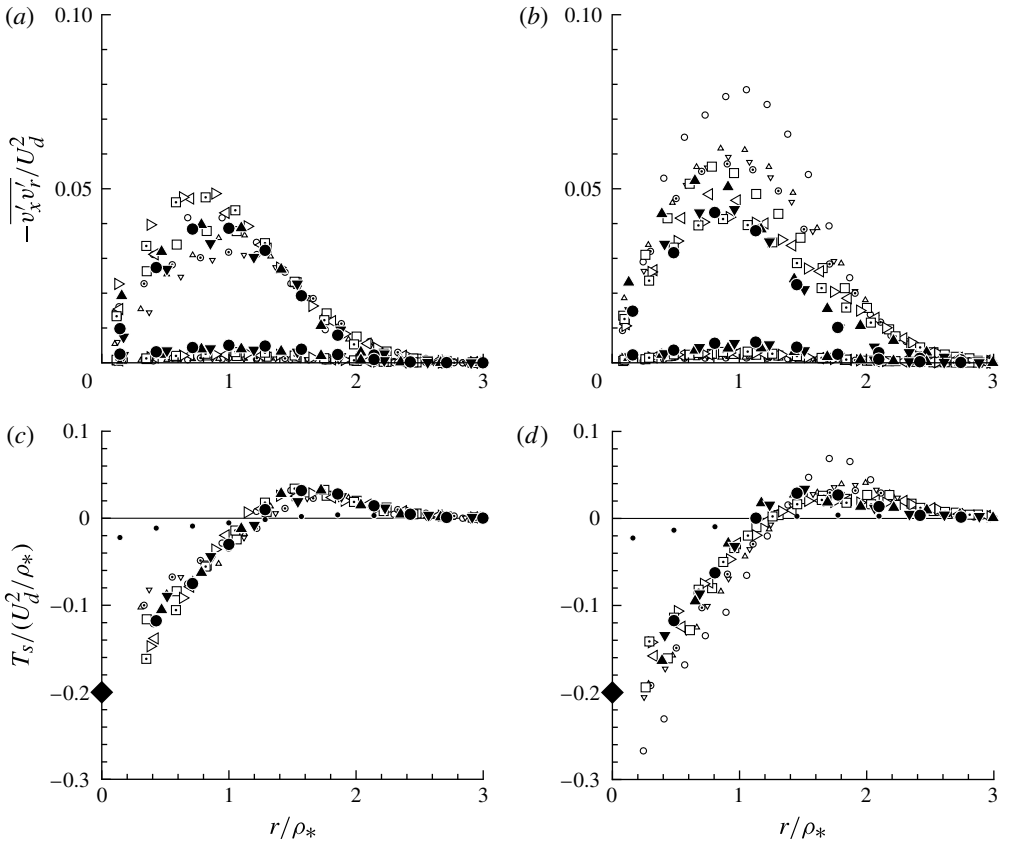


FIGURE 18. Profiles of shear stress and terms in RANS equation: (*a*,*c*) Case VR, $t/t_* =$: ○, 334; △, 708; ▽, 960; ⊙, 1299; □, 2135; ◁, 2832; ▷, 3591; ⊡, 4386; ▲, 9308; ▼, 20 272; ●, 30 964. (*b*,*d*) Case SD, $t/t_* =$: ○, 366; △, 622; ▽, 936; ⊙, 1272; □, 1962; ◁, 2544; ▷, 3218; ⊡, 3930; ▲, 9437; ▼, 19 947; ●, 30 920. The upper and lower symbols in (*a*,*b*) respectively show the Reynolds $-\overline{v_x' v_r'}$ and viscous $\nu\,\partial\overline{v}_x/\partial r$ stress profiles. In (*c*) and (*d*) the larger symbols indicate $T_s$, the sum of the Reynold-stress $T_t$ and viscous $T_v$ terms in the RANS equation (as in figure 11), while the smaller symbols (•) show $T_v$ at (*c*) $t/t_* = 30\,964$ (VR) and (*d*) $t/t_* = 30\,920$ (SD), and the larger symbol (⧫) at $r = 0$ is $\mathrm{d}U_d/\mathrm{d}t$ from linear curve-fit of $U_d^{-3/2}$ history shown in figure 15(*a*), which implies $\mathrm{d}U_d/\mathrm{d}t = -A\ (\ln 2/\pi)^{1/2}(2/3\rho_{*o})\ (I_d/U_{do})^{1/2}(U_d^2/\rho_*)$ with $A = 0.30$.

at these times. However, $T_v/T_t$ being small is consistent with, and in fact required for, the $n = 1/3$ mean-flow behaviour seen in figure 15(*a*,*b*).

Perhaps it should also be mentioned that the $U_d^{-1/2n}$ histories considered by JGG, who for the $U_d\,\delta_*/\nu < 250$ range chose $n = 1/2$ (see their figure 14*b*,*d*), would be only marginally less linear if $n = 1/3$ had been chosen instead. In view of the present findings it is conceivable that the late-time Gourlay *et al.* data would agree more closely with the high-Reynolds-number ($n = 1/3$) solution if a less uncertain measure of $U_d$ had been used for their comparison. (It must be admitted that the present $n = 1/3$ fits would also be only marginally worse if $n = 1/2$ were used, but such behaviour would not be consistent with other aspects of the data, nor the analysis of § 3.) Moreover, note that $(\overline{v_x' v_x'})^{1/2}/U_d \approx 0.2$ (identified by JGG as characteristic

https://doi.org/10.1017/jfm.2012.371 Published online by Cambridge University Press

of $n = 1/2$ similarity) is only present in one of the two Gourlay traces (crosses) in figure 16(*a*) (from vertical and horizontal planes through the domain centreline) and that this only appears at very late times when (as noted above) the flow is susceptible to being unphysically laminarized by the too-small domain. Laminarization is also suggested by the apparently perfect Gaussian behaviour of the mean velocity profile displayed in JGG's figure 15, and also found here (but not shown) for Case VR for $t/t_* > 10^6$.

Despite these misgivings, we find that the central claim of the JGG equilibrium similarity analysis – that self-similarity need not be universal – is unambiguously supported by the present results, in that wakes created with the same net momentum defect but different initial structure (corresponding to generating bodies of different geometries) exhibit non-universal self-similarity, characterized by different mean spreading rates and energy levels that retain their initial-condition dependence. But we emphasize that the present DNS data reveal that eventually the two wakes both reach the classical universal state.

Finally, we consider the eddy-viscosity profiles in figure 19. The variation in (*a*) and (*b*) is consistent with the $n = 1/3$ state, in that $\widetilde{\nu}_t/\nu \gg 1$ throughout the period of universal behaviour. The $n = 1/3$ solution is also indicated by the history of $\widetilde{\nu}_t$ at $r = \rho_*$, denoted $\widetilde{\nu}_*$, which is plotted for Case SD (for which the statistics are most reliable) in the inset in figure 19(*b*). Since $\nu_t/\nu \propto t^{2n-1}$, the linear variation with time of $(\widetilde{\nu}_*)^{-3}$ confirms that despite its low Reynolds number, the flow is still within the $n = 1/3$ regime. When the eddy viscosity is scaled by $U_d\,\rho_*$ rather than $\nu$ (figure 19*c*,*d*), it again favours $n = 1/3$ over $n = 1/2$ (albeit in a less compelling manner), since it comes closer to remaining constant in time than it does to increasing (recall that the similarity theory predicts $\nu_t/U_d\rho_* \propto t^{3n-1}$). We also observe from figure 19(*c*,*d*) that for the universal regime, in the core region, $\nu_t/U_d\rho_* \approx 0.06$, which corresponds to a turbulence Reynolds number $R_T = U_d\,\delta_*/\nu_t$ of $(\delta_*/\rho_*)/(0.06) \approx 14$ – remarkably close to Tennekes & Lumley's (1972) proposal of $R_T = 14.1$ for axisymmetric wakes. Profiles of $k^2/\epsilon$, which can also be interpreted as an eddy viscosity, are presented in figure 19(*e*,*f*); these indicate that in the core region during the universal state $k^2/\epsilon U_d\rho_* \approx 0.3$, which in turn implies (when compared to the $\nu_t/U_d\rho_*$ profiles) that $C_\mu$, a crucial coefficient in the well-known $k$–$\epsilon$ RANS turbulence model, is roughly 0.2. This is over twice the value typically used, so on that basis alone 'classical' $k$–$\epsilon$ would not return the universal wake identified here.

## 5. Summary and closing remarks

The major conclusion is that axisymmetric turbulent wakes with very different initial conditions eventually reach a universal, self-similar state that matches the well-known solution (for which, for example, the wake width grows like $t^{1/3}$). This was Townsend's classical hypothesis. Evidence for the final universal form appears first in the mean-defect history, as the universal structure develops first near the central region of the wake, growing slowly towards its outer edge. Once this growth towards universality is complete it is not possible to discern from any feature of the wake what the initial conditions were – the flow has genuinely lost all memory of how it was initiated. However, such universality only appears here after very long times (when the maximum velocity is only about 1 % of its initial value) or, equivalently, extremely long distances downstream – so far, in fact, as to suggest such a wake may in general not be seen in practice, unless its initialization is very close to the universal state. This is illustrated by the fact that, in the spatially developing equivalent

https://doi.org/10.1017/jfm.2012.371 Published online by Cambridge University Press

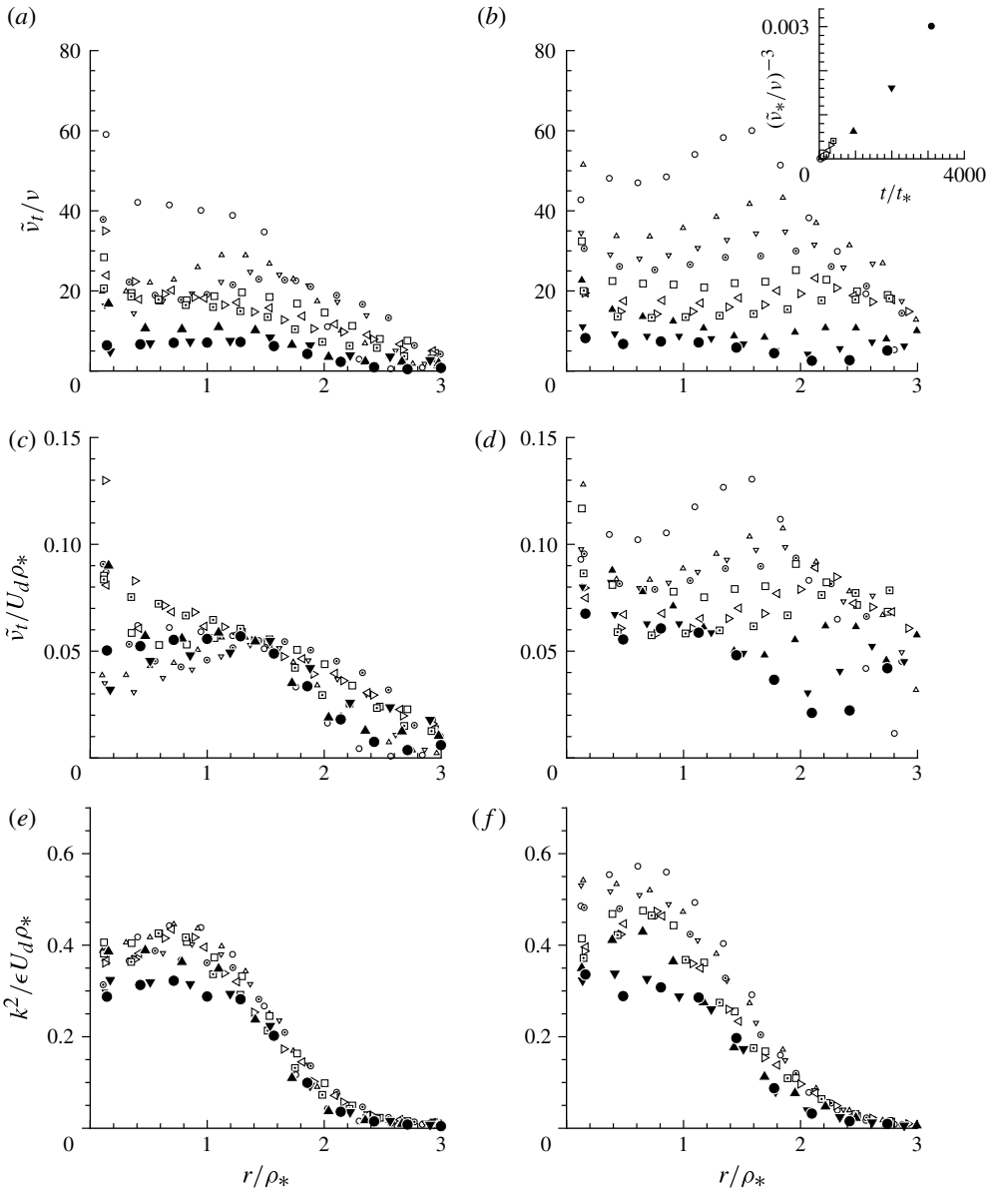


FIGURE 19. Profiles of (*a–d*) eddy viscosity diagnostic $\widetilde{\nu}_t = [-\overline{v_x' v_r'}/(\partial G/\partial r)]$, where $G$ is the Gaussian mean-velocity profile, such that $\partial G/\partial r = (2 \ln 2\, U_d r/\rho_*^2) \exp(-\ln 2\, (r/\rho_*)^2)$, and (*e,f*) $k^2/\epsilon$: (*a,c,e*) Case VR, $t/t_* =$: ○, 334; △, 708; ▽, 960; ⊙, 1299; □, 2135; ◁, 2832; ▷, 3591; ⊡, 4386; ▲, 9308; ▼, 20 272; ●, 30 964. (*b,d,f*) Case SD, $t/t_* =$: ○, 366; △, 622; ▽, 936; ⊙, 1272; □, 1962; ◁, 2544; ▷, 3218; ⊡, 3930; ▲, 9437; ▼, 19 947; ●, 30 920. Inset plot in (*b*) shows the history for Case SD of $\widetilde{\nu}_*$, the value of $\widetilde{\nu}_t$ at $r = \rho_*$.

of our time-dependent wakes, a 2.5 cm generating body would not reach universality until nearly 100 m downstream. (The question of the precise relationship between the

https://doi.org/10.1017/jfm.2012.371 Published online by Cambridge University Press

details, e.g. low-wavenumber content, of the initial conditions and the time required for the universal state to develop is deferred to a future study. Factors such as the size of the streamwise domain may affect the development time, although not we presume by enough to alter the general conclusions drawn from the present results.)

At earlier times (or distances) non-universal self-similar behaviour appears; this has the same mean growth-rate behaviour ($\delta \sim t^{1/3}$), but the proportionality constant is dependent on initial conditions, as found by other authors (e.g. Bevilaqua & Lykoudis 1978; Johansson *et al.* 2003). In general, the present DNS results support Johansson *et al.*'s conclusions, for example their prediction that the Reynolds-stress profiles scale with $U_d^2\beta$, with the growth rate $\beta = (1/U_d)\,\mathrm{d}\delta/\mathrm{d}t$ different for different initial conditions. In the eventual universal regime, however, $\beta$ is independent of initial conditions, with $\beta \approx 0.10$.

The time required for both non-universal and universal versions of self-similarity to appear depends, not surprisingly perhaps, on the initial conditions. When a vortex-ring structure is imposed at $t = 0$, the non-universal self-similar state (corresponding to what Narasimha (1992) called 'metastable equilibrium') is reached earlier and at higher Reynolds number than when using low-level random-phase disturbances. In the non-ring case, transition and wake turbulence arise from the development of linearly unstable (helical) modes, rather than from the azimuthal instabilities arising in the vortex rings. The vortex-ring initialization yields $\beta = 0.06$, compared with the significantly faster growth rate, $\beta = 0.13$, found for the less structured initial condition. The latter value is, interestingly, close to that found by Gourlay *et al.* (2001), who used much larger-amplitude initial perturbations so that the initial transition was via nonlinear perturbations. Paradoxically, universal self-similarity is achieved at about the same time by both wakes, although one takes longer to become turbulent, and to experience (non-universal) self-similarity.

The universal wake behaviour appears and is maintained at unexpectedly low values of the wake Reynolds number, $U_d\,\delta_*/\nu$, down to at least 100 (much less than the 500 suggested by Johansson *et al.* (2003) as the value below which $n = 1/2$-type behaviour would appear). It turns out that $\beta$ is sufficiently constant to imply the $n = 1/3$ behaviour directly from dimensional analysis (based on Townsend's hypothesis), and we have shown that a fully turbulent wake (for which $\nu_t/\nu \gg O(1)$) cannot yield $n = 1/2$ behaviour unless the eddy viscosity is constant with respect to time, which here it is not (cf. JGG). Even at times corresponding to $O(10^5)$ diameters downstream of an equivalent virtual body, the viscous term in the Reynolds-averaged Navier–Stokes equation remains an order of magnitude smaller than the Reynolds-stress term, and $\nu_t/\nu$ decreases according to the $n = 1/3$ scaling. Very much later, when the streamwise size of the computational domain becomes too small, the flow becomes purely laminar (due to constraint of the large-eddy structures) and a genuine $n = 1/2$, Gaussian wake appears. (We believe this may be the cause of the $n = 1/2$ behaviour in the late-time Gourlay *et al.* (2001) data, presented in JGG.) It is worth recalling here that $n = 1/2$ behaviour was seen at very early times in the vortex-ring case; this was a result of the essentially radially uniform and steady eddy viscosity in the central part of the wake, consistent with the argument above. However, it quickly disappeared as the self-similar turbulence structure developed, leading to unsteady $\nu_t$, and the wake entered the more long-lasting $n = 1/3$ self-similar but non-universal state.

Comparison of figure 12(*e*,*f*) with figure 18(*c*,*d*) reveals that as time passes the viscous stress becomes increasingly significant relative to the turbulent stress. This leads one to consider the final state of the flow in the extreme $t \to \infty$ limit. It is

https://doi.org/10.1017/jfm.2012.371 Published online by Cambridge University Press

conceivable that eventually the viscous and turbulent terms in the RANS equation become of the same order, allowing the $n = 1/2$ regime to emerge. Computational constraints have not allowed us to pursue the question of whether or not the flow could ever naturally (that is, not as a result of a too small numerical domain) become purely laminar, and move from the first to the second $n = 1/2$ solution discussed in § 2.

Another issue that has not been pursued concerns the way that the non-universal self-similar flows are slowly 'pulled away' from their initial-condition-dependent states towards the universal behaviour. This would require examination of the evolution of the different terms in the shear-stress transport equation. It might also be worth examining whether more physically based turbulence modelling approaches (e.g. detached or large-eddy simulation) can reproduce the non-universal wake behaviour. What seems certain is that classical RANS closures will not.

## Acknowledgements

This work was supported by the UK Ministry of Defence (Dstl project RD027-02854, managed by Dr R. P. Hornby), and the UK Turbulence Consortium, funded by the EPSRC under Grants EP/D044073/1 and EP/G069581/1. It made use of the facilities of HPCx and HECToR, the UK's national high-performance computing service, which is provided by UoE HPCx Ltd at the University of Edinburgh, Cray Inc and NAG Ltd, and funded by the Office of Science and Technology through EPSRC's High End Computing Programme. We are indebted to Drs P. J. Archer, T. S. Lund, E. Rind, K. Shariff and T. G. Thomas, and Professors S. Chernyshenko, B. Ganapathisumbramani, R. D. Sandberg and N. D. Sandham for their advice and encouragement along the way. Professors P. Bradshaw and R. Narasimha made useful comments on the manuscript. Thanks are due Dr C. P. Yorke for the substantial role he played in developing the vortex-ring initialization strategy, and to Dr Lund for proposing the procedure used to expand the lateral domain. The explanation in § 3 regarding the relationship between the radius of the vortex rings and the half-width of the initial mean profile was provided by Dr Shariff. We have also benefited from timely discussions with Professor W. K. George, Professor J. C. R. Hunt, Dr M. M. Rogers and especially Dr P. R. Spalart.

## REFERENCES

ARCHER, P. J., THOMAS, T. G. & COLEMAN, G. N. 2008 Direct numerical simulations of vortex ring evolution from laminar to the early turbulent regime. *J. Fluid Mech.* **598**, 201–206.

BASU, A. J., NARASIMHA, R. & SINHA, U. N. 1992 Direct numerical simulation of the initial evolution of a turbulent axisymmetric wake. *Curr. Sci.* **63**, 734–740.

BEVILAQUA, P. M. & LYKOUDIS, P. S. 1978 Turbulence memory in self-preserving wakes. *J. Fluid Mech.* **89** (3), 589–606.

CANNON, S. F. & CHAMPAGNE, F. 1991 Large-scale structures in wakes behind axisymmetric bodies. In *Proceedings Eighth Symposium on Turbulent Shear Flows, Munich*, pp. 6.5.1–6.5.6.

CHEVRAY, R. 1968 The turbulent wake of a body of revolution. *Trans. ASME: J. Basic Engng* **90**, 275–284.

DOMMERMUTH, D. G., ROTTMAN, J. W., INNIS, G. E. & NOVIKOV, E. A. 2002 Numerical simulation of the wake of a towed sphere in a weakly stratified fluid. *J. Fluid Mech.* **473**, 83–101.

EWING, D., GEORGE, W. K., ROGERS, M. M. & MOSER, R. D. 2007 Two-point similarity in temporally evolving plane wakes. *J. Fluid Mech.* **577**, 287–307.

https://doi.org/10.1017/jfm.2012.371 Published online by Cambridge University Press

GEORGE, W. K. 1989 The self-preservation of turbulent flows and its relation to initial conditions and coherent structure. In *Advances in Turbulence* (ed. W. K. George & R. Arndt), pp. 39–73. Hemisphere.

GEORGE, W. K. 2008 Freeman Lecture: Is there an asymptotic effect on initial and upstream conditions on turbulence? FEDSM2008-55362. In *Proceedings of ASME 2008 Fluids Engineering Meeting*, pp. 1–26. ASME.

GEORGE, W. K. & DAVIDSON, L. 2004 Role of initial conditions in establishing asymptotic flow behaviour. *AIAA J.* **42** (3), 438–446.

GOTTLIEB, D. & ORSZAG, S. A. 1977 *Numerical Analysis of Spectral Methods: Theory and Applications*. SIAM.

GOURLAY, M. J., ARENDT, S. C., FRITTS, D. C. & WERNE, J. 2001 Numerical modelling of initially turbulent wakes with net momentum. *Phys. Fluids* **13** (12), 3783–3802.

JIMÉNEZ, J. & MOIN, P. 1991 The minimal flow unit in near-wall turbulence. *J. Fluid Mech.* **225**, 213–240.

JOHANSSON, P. B. V., GEORGE, W. K. & GOURLAY, M. J. 2003 Equilibrium similarity, effects of initial conditions and local Reynolds number on the axisymmetric wake. *Phys. Fluids* **15** (3), 603–617.

KIM, J., MOIN, P. & MOSER, R. 1987 Turbulence statistics in fully developed channel flow at low Reynolds number. *J. Fluid Mech.* **177**, 133–166.

MOSER, R. D., ROGERS, M. M. & EWING, D. W. 1998 Self-similarity of time-evolving plane wakes. *J. Fluid Mech.* **367**, 255–289.

NARASIMHA, R. 1992 The utility and drawbacks of traditional approaches. In *Whither Turbulence?* (ed. J. Lumley). pp. 13–49. Springer.

NARASIMHA, R. & PRABHU, A. 1972 Equilibrium and relaxation in turbulent wakes. *J. Fluid Mech.* **54**, 1–17.

POPE, S. B. 2000 *Turbulent Flows*. Cambridge University Press.

ROGALLO, R. S. 1981 Numerical experiments in homogeneous turbulence. NASA Technical Memorandum 81315.

SANDHAM, N. D. 2002 Introduction to direct numerical simulation. In *Closure Strategies for Turbulent and Transitional Flows* (ed. B. E. Launder & N. D. Sandham). pp. 248–266. Cambridge University Press.

SHARIFF, K., VERZICCO, R. & ORLANDI, P. 1994 Three-dimensional vortex ring instabilities. *J. Fluid Mech.* **279**, 351–375.

SPALART, P. E., MOSER, R. D. & ROGERS, M. M. 1991 Spectral methods for the Navier–Stokes equations with one infinite and two periodic directions. *J. Comput. Phys.* **96** (2), 297–324.

SREENIVASAN, K. R. 1981 Approach to self-preservation in plane turbulent wakes. *AIAA J.* **19**, 1365–1367.

SREENIVASAN, K. R. & NARASIMHA, R. 1982 Equilibrium parameters for two-dimensional turbulent wakes. *Trans. ASME: J. Fluids Engng* **104**, 167–170.

TENNEKES, H. & LUMLEY, J. L. 1972 *A First Course in Turbulence*. MIT.

TOWNSEND, A. A. 1956 *The Structure of Turbulent Shear Flow*. Cambridge University Press.

TOWNSEND, A. A. 1976 *Structure of Turbulent Shear Flow*, 2nd edn. Cambridge University Press.

ZHOU, Y. & ANTONIA, R. A. 1995 Memory effects in a turbulent plane wake. *Exp. Fluids* **19**, 112–120.

https://doi.org/10.1017/jfm.2012.371 Published online by Cambridge University Press